Mathematical Biosciences 368 (2024) 109128

Contents lists available at ScienceDirect

Mathematical Biosciences

journal homepage: www.elsevier.com/locate/mbs

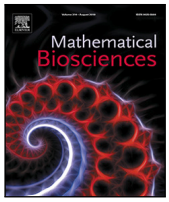

Original Research Article

Travelling waves due to negative plant–soil feedbacks in a model including tree life-stages

Annalisa Iuorio [a,b], Mara Baudena [c,d,e], Maarten B. Eppinga [f], Francesco Giannino [g], Max Rietkerk [c], Frits Veerman [h,*]

[a] University of Vienna, Faculty of Mathematics, Oskar-Morgenstern-Platz 1, Vienna, 1090, Austria
[b] Parthenope University of Naples, Department of Engineering, Centro Direzionale - Isola C4, Naples, 80143, Italy
[c] Utrecht University, Copernicus Institute of Sustainable Development, Environmental Sciences Group, Utrecht, 3508 TC, The Netherlands
[d] National Research Council of Italy, Institute of Atmospheric Sciences and Climate (CNR-ISAC), Corso Fiume 4, Torino, 10133, Italy
[e] National Biodiversity Future Center, Piazza Marina, 61, Palermo, 90133, Italy
[f] University of Zurich, Department of Geography, Winterthurerstrasse 190, Zürich, 8057, Switzerland
[g] University of Naples Federico II, Department of Agricultural Sciences, via Università 100, Portici, 80055, Italy
[h] Leiden University, Mathematical Institute, Niels Bohrweg 1, Leiden, 2300 RA, The Netherlands

ARTICLE INFO

MSC:
35C07
34C60
34D05
35K57
37C25
65M06
92D40

Keywords:
Reaction–diffusion-ODE
Janzen–Connell hypothesis
Autotoxicity
Travelling waves
Linear spreading speed
Negative feedback

ABSTRACT

The emergence and maintenance of tree species diversity in tropical forests is commonly attributed to the Janzen–Connell (JC) hypothesis, which states that growth of seedlings is suppressed in the proximity of conspecific adult trees. As a result, a JC distribution due to a density-dependent negative feedback emerges in the form of a (transient) pattern where conspecific seedling density is highest at intermediate distances away from parent trees. Several studies suggest that the required density-dependent feedbacks behind this pattern could result from interactions between trees and soil-borne pathogens. However, negative plant–soil feedback may involve additional mechanisms, including the accumulation of autotoxic compounds generated through tree litter decomposition. An essential task therefore consists in constructing mathematical models incorporating both effects showing the ability to support the emergence of JC distributions.

In this work, we develop and analyse a novel reaction–diffusion-ODE model, describing the interactions within tropical tree species across different life stages (seeds, seedlings, and adults) as driven by negative plant–soil feedback. In particular, we show that under strong negative plant–soil feedback travelling wave solutions exist, creating transient distributions of adult trees and seedlings that are in agreement with the Janzen–Connell hypothesis. Moreover, we show that these travelling wave solutions are pulled fronts and a robust feature as they occur over a broad parameter range. Finally, we calculate their linear spreading speed and show its (in)dependence on relevant nondimensional parameters.

1. Introduction

A widely observed phenomenon in forest tree communities is that conspecific seedling density is highest at intermediate distances from the parent tree, referred to as the Janzen–Connell (JC) distribution. The emergence of JC distributions provide an explanation for the creation and maintenance of high species diversity in forest tree communities [1,2]. This (transient) pattern is particularly important in terms of biodiversity: the space between the parent tree and its seedlings is a favourable area for other species to colonise and grow, enhancing coexistence (see e.g. [3,4]).

From an ecological viewpoint, an increasing number of ecological studies is supporting the idea that the emergence of this pattern (particularly prominent in tropical ecosystems) is strongly linked to negative plant–soil feedbacks [5–7]. Among the main mechanisms responsible for such feedbacks, the accumulation of species-specific soil pathogens is indicated as prominent [5,8]. Consequently, several models have been introduced in the last few decades to theoretically investigate this mechanism (see e.g. [9–12] and references therein). In recent years, additional mechanisms generating negative plant–soil feedback have been identified, including the accumulation of conspecific extracellular DNA fragments leading to an autotoxic soil environment [13,14]. Such

* Corresponding author.
E-mail addresses: annalisa.iuorio@univie.ac.at (A. Iuorio), m.baudena@isac.cnr.it (M. Baudena), maarten.eppinga@geo.uzh.ch (M.B. Eppinga), giannino@unina.it (F. Giannino), M.G.Rietkerk@uu.nl (M. Rietkerk), f.w.j.veerman@math.leidenuniv.nl (F. Veerman).

https://doi.org/10.1016/j.mbs.2023.109128
Received 9 June 2023; Received in revised form 6 November 2023; Accepted 8 December 2023
Available online 20 December 2023

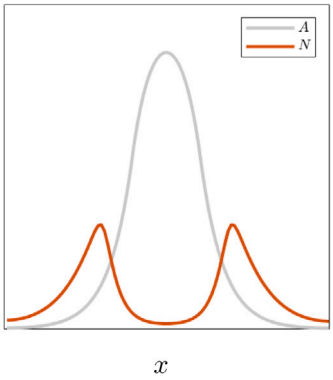

Fig. 1. Schematic representation of a one-dimensional section of a Janzen–Connell distribution. Here, the typical seedlings' density distribution N (orange curve) is symmetrically travelling towards the boundary of the domain and exhibiting a depression in the centre, where the peak of the adults' density A (grey curve) is reached.

negative feedback induced by autotoxicity could potentially explain species coexistence in diverse communities [15–17] as well as plants spatial organisation by means of as clonal rings [18,19], fairy rings [20,21], and more generally vegetation patterns [22,23]. The spatial distribution of adult forest trees and their seedlings is the outcome of different ecological processes. On the one hand, deposition of seeds on the ground will be higher near the adult parent tree, and decrease with increasing distance from the parent tree. On the other hand, seed and seedling survival may also depend on the presence of adult trees, with empirical observations suggesting that mortality is highest in close proximity of the adults of the parent tree species [1,2]. As a result of these two types of processes, the density of seedlings is expected to be highest at intermediate distances from the parent tree (Fig. 1), a distribution referred to in the ecological literature as the Janzen–Connell hypothesis. In the specific case considered here, we would expect negative feedback to strongly diminish seed and seedling density close to parental trees, with the surviving seedlings reaching maturity. In space, this process may be reflected by a travelling wave of high seedling density.

In this work, we construct a new model based on reaction–diffusion-ODEs in order to describe the emergence of JC distributions including both growth inhibition (induced by extracellular self-DNA) and increased mortality (mainly linked to the accumulation of soil-borne pathogens). Reaction–diffusion-ODE systems are used to model a wide variety of phenomena in biology; however, only few analytical results concerning their behaviour – which often strongly differs from classical reaction–diffusion models – are available, see e.g. [24–28].

As both growth inhibition and increased mortality mechanisms act on different tree life-stages, we consider a stage-structured framework. Our aim consists in introducing a theoretical tool which may help assessing the relative contribution of both mechanisms to emergent spatial distributions of adult trees and their seedlings. As JC distributions are experimentally observed as transient patterns, we analytically investigate the existence of travelling wave solutions which exhibit the typical JC feature of seedlings' biomass being at a maximum at suitable distances from the parent tree. Travelling wave solutions are widely found in mathematical models inspired by several biological applications, including e.g. species competition [29], tumour growth [30], and bacterial chemotaxis [31]. In particular, we show the existence of such solutions and derive corresponding relevant properties. Moreover, we hypothesise that the constructed travelling wave solutions correspond to pulled fronts, whose speed then coincides with the linear speed determined by a linear analysis near the trivial steady state. We then analytically derive the linear speed and confirm our prediction by comparing the analytical value with the one obtained by numerical simulations of our model for a set of fixed parameter values and investigating their dependence with respect to two relevant parameters.

The impact of the work presented here is twofold: from the ecological viewpoint, our work provides a valuable theoretical tool to further address relevant issues related to JC distributions (e.g. understanding how the dispersal ability of tree species moderate the spatial patterns of adult and seedlings and to what extent are plant strategies along the growth-defence trade-off reflected in the spatial patterns of adult and seedlings). From the mathematical viewpoint, on the other hand, the analytical strategy used here to investigate travelling waves in a system of 4 reaction–diffusion-ODEs improves our understanding of such complex systems and offers a framework potentially useful to investigate problems exhibiting a similar structure.

The paper is structured as follows: in Section 2 we introduce the model both in its dimensional and nondimensional form, on which we focus for our subsequent analysis. The spatially homogeneous steady states associated to this model are derived in Section 3. In Section 4 the linear stability of these steady states with respect to both homogeneous and heterogeneous perturbations is carried out, revealing the absence of Turing patterns for the parameter ranges defined based on experimental findings (as expected). The existence and the main properties of travelling wave solutions (in particular right-moving fronts) are then investigated in Section 5: numerical simulations suggesting the existence of pulled fronts are corroborated analytically by deriving the linear wave speed and comparing it with the numerical measured speed. We conclude our work with a discussion of the results obtained and an outlook indicating further research perspectives in Section 6.

2. The model

In our framework, negative plant–soil feedback (NF) manifests itself both during the seed-to-seedling transition (in terms of *growth inhibition*) and at the seedlings life-stage (in terms of *increased mortality*). The first effect can be often attributed to the presence of extracellular self-DNA (also known as autotoxicity), whereas the second effect is mainly linked to soil-borne pathogens. As these factors act at different stages of a tree lifespan, vegetation is considered in terms of biomass and is divided into three compartments corresponding to three different life-stages, namely seeds $\hat{S}$ ($\mathrm{kg/m^2}$), seedlings $\hat{N}$ ($\mathrm{kg/m^2}$) and adults $\hat{A}$ ($\mathrm{kg/m^2}$). Moreover, the general inhibitor variable $\hat{I}$ ($\mathrm{kg/m^2}$) represents the density of inhibitor responsible both for growth inhibition and increased mortality effects. The interaction of such variables at any spatial point $\hat{\mathbf{x}} = (\hat{x}, \hat{y})$ and any time $\hat{t}$ is based on the following assumptions: the increase of seed density is influenced by adult tree production via the per capita seed production rate $\hat{g}_S$ and seed dispersal $\hat{d}_S$, whereas their natural decay rate (including predation) is represented by $\hat{k}_S$. Seeds then germinate and the seedlings might establish or not, depending also on the inhibitor due to the effect of autotoxicity via the function $\frac{\hat{g}_N \hat{S}}{1+\gamma\, e^{\hat{r}_T \hat{I}}}$. This monotonically decreasing logistic function (see [32]) models the fact that low autotoxicity values do not affect the base establishment probability ($\hat{g}_N$), whereas this probability converges to zero as autotoxicity increases with a speed determined by the species' sensitivity to autotoxicity ($\hat{r}_T$). Seedlings have a natural turnover rate $\hat{k}_N$, enhanced by pathogens via the term $\hat{r}_P \hat{I}$. The seedlings which survive then grow into the next life stage according to the function $\hat{g}_A \left(1 - \frac{\hat{A}}{\hat{A}_{\max}}\right)$. Adults' density grows logistically because of seedlings transitioning to the adult stage at rate $\hat{g}_A$, intrinsic growth rate $\hat{c}_A$, and constant per capita mortality rate $\hat{k}_A$. The inhibitor density grows due to adult decomposition byproducts at a rate $\hat{c}_T$, decays naturally at a rate $\hat{k}_I$, and diffuses in the soil at a rate determined by the coefficient $\hat{d}_I$. These ecological processes are described by the following PDE-ODE

Table 1
Description, values, and units for model parameters in System (1), obtained through parametrisation and calibration.

Parameter	Description	Value	Units
$\hat{g}_S$	Growth rate of $\hat{S}$	$6.67 \cdot 10^{-8} - 0.033$	y^{-1}
$\hat{k}_S$	$\hat{S}$ turnover rate	0.33–0.5	y^{-1}
$\hat{g}_N$	Transition rate from $\hat{S}$ to $\hat{N}$	0.25–25	y^{-1}
γ	Establishment sensitivity to toxicity parameter	10^{-5}	–
$\hat{r}_T$	Establishment sensitivity to toxicity parameter	0–68	$m^2\ kg^{-1}$
$\hat{k}_N$	Death rate of $\hat{N}$	0.02–0.74	y^{-1}
$\hat{r}_P$	Extra mortality of $\hat{N}$ caused by $\hat{I}$	0–2	$m^2\ kg^{-1}\ y^{-1}$
$\hat{g}_A$	Transition rate from $\hat{N}$ to $\hat{A}$	0.02–1	y^{-1}
$\hat{c}_A$	Growth rate in $\hat{A}$'s biomass density	0.25	y^{-1}
$\hat{A}_{\max}$	Maximum capacity for $\hat{A}$	30	$m^{-2}\ kg$
$\hat{k}_A$	Mortality rate of $\hat{A}$	0.01	y^{-1}
$\hat{c}_I$	Growth rate of $\hat{I}$ due to $\hat{A}$	1	y^{-1}
$\hat{k}_I$	Inhibitor decay rate	0.7	y^{-1}
$\hat{d}_S$	Diffusion coefficient for $\hat{S}$	0.6–4	$m^2\ y^{-1}$
$\hat{d}_I$	Diffusion coefficient for $\hat{I}$	0–0.5	$m^2\ y^{-1}$

system:

$$\begin{aligned}
\frac{\partial \hat{S}}{\partial \hat{t}} &= \hat{d}_S\,\Delta\hat{S} + \hat{g}_S\,\hat{A} - \hat{k}_S\,\hat{S},\\
\frac{\partial \hat{N}}{\partial \hat{t}} &= \frac{\hat{g}_N\,\hat{S}}{1+\gamma\,e^{\hat{r}_T\,\hat{I}}} - \left(\hat{k}_N + \hat{g}_A\left(1-\frac{\hat{A}}{\hat{A}_{\max}}\right) + \hat{r}_P\,\hat{I}\right)\hat{N},\\
\frac{\partial \hat{A}}{\partial \hat{t}} &= \left(\hat{g}_A\,\hat{N} + \hat{c}_A\,\hat{A}\right)\left(1-\frac{\hat{A}}{\hat{A}_{\max}}\right) - \hat{k}_A\,\hat{A},\\
\frac{\partial \hat{I}}{\partial \hat{t}} &= \hat{d}_I\,\Delta\hat{I} + \hat{c}_I\,\hat{A} - \hat{k}_I\,\hat{I}.
\end{aligned} \tag{1}$$

The PDEs for the seed biomass $\hat{S}$ and the inhibitor biomass $\hat{I}$ are of reaction–diffusion type. Values and meaning of the non-negative model parameters in (1) are provided in Table 1. Based on an ecological investigation, they have been calibrated in some cases and parametrised in all the others [33]. We note here that the model in Eq. (1) has been developed for a wide range of possible types of domains and initial/boundary conditions; hence we keep these general at this stage of the paper.

In this framework, links to the Janzen–Connell hypothesis can be found in transient patterns where a ring of seedlings emerges around the adult tree (whose density is concentrated in the centre of the ring). Mathematically, this consists in travelling wave solutions, whose construction we analyse in this work. From here on, we refer to this phenomenon as the Janzen–Connell distribution.

In order to reduce the total number of parameters and to facilitate the analytical investigation of our model, we introduce a nondimensional version of System (1). Existence and stability (both under homogeneous and heterogeneous perturbations) of the corresponding steady states are then investigated in Sections 3 and 4, respectively.

In order to facilitate the investigation of the existence and stability properties of our model, we introduce the following nondimensional variables:

$$\begin{gathered}
t = \hat{c}_A\,\hat{t}, \quad x = \sqrt{\frac{\hat{c}_A}{\hat{d}_S}}\,\hat{x}, \quad y = \sqrt{\frac{\hat{c}_A}{\hat{d}_S}}\,\hat{y},\\
S = \frac{\hat{c}_A}{\hat{g}_S\,\hat{A}_{\max}}\,\hat{S}, \quad N = \frac{\hat{c}_A}{\hat{g}_N\,\hat{A}_{\max}}\,\hat{N}, \quad A = \frac{\hat{A}}{\hat{A}_{\max}}, \quad I = \frac{\hat{c}_A}{\hat{c}_I\,\hat{A}_{\max}}\,\hat{I}.
\end{gathered} \tag{2}$$

We choose $\hat{c}_A$, the growth rate of the adult biomass density, as the characteristic time scale; this adult growth rate can often be experimentally and/or observationally determined in a manner (relatively) independent from other process factors (see e.g. [34]). In addition, we choose the resulting characteristic seed dispersal distance as the characteristic length scale. For every model variable, the biomass density is scaled relative to the adult carrying capacity $\hat{A}_{\max}$. Furthermore, for algebraic convenience, all nondimensionalised model variables are divided by ratio of that variable's growth rate relative to the characteristic growth rate $\hat{c}_A$.

Table 2
Description and ranges of rescaled nondimensional parameters used in System (3), based on Table 1.

Parameter	Description	Value
k_S	S turnover rate	1.3–2.0
g_S	Growth rate of S	$2.7 \cdot 10^{-7} - 1.3 \cdot 10^{-1}$
γ	Establishment sensitivity to toxicity parameter	$1.0 \cdot 10^{-5}$
r_T	Establishment sensitivity to toxicity parameter	$0–0.8 \cdot 10^4$
k_N	Death rate of N	$0.8 \cdot 10^{-1} - 3.0$
r_P	Increased mortality of N caused by I	$0–1.0 \cdot 10^3$
g_A	Transition rate from N to A	$0.8 \cdot 10^{-3} - 4.0$
k_A	Mortality rate of A	$4.0 \cdot 10^{-2}$
g_N	Transition rate from S to N	$1.0–1.0 \cdot 10^2$
k_I	Inhibitor decay rate	2.8
d	Square root of diffusion ratio	0–0.9

This leads to the following nondimensional reformulation of Eq. (1)

$$\begin{aligned}
\frac{\partial S}{\partial t} &= \Delta S + A - k_S\,S,\\
\frac{\partial N}{\partial t} &= \frac{g_S\,S}{1+\gamma\,e^{r_T I}} - N\,\left(k_N + r_P\,I + g_A\,(1-A)\right),\\
\frac{\partial A}{\partial t} &= A\,(1-k_A-A) + g_A\,g_N\,N\,(1-A),\\
\frac{\partial I}{\partial t} &= d^2\,\Delta I + A - k_I\,I,
\end{aligned} \tag{3}$$

where $\Delta = \frac{\partial^2}{\partial x^2} + \frac{\partial^2}{\partial y^2}$ and the nondimensional parameters are given by

$$\begin{gathered}
k_S = \frac{\hat{k}_S}{\hat{c}_A}, \quad k_N = \frac{\hat{k}_N}{\hat{c}_A}, \quad r_P = \frac{\hat{r}_P\,\hat{c}_I\,\hat{A}_{\max}}{\hat{c}_A^2}, \quad k_A = \frac{\hat{k}_A}{\hat{c}_A}, \quad k_I = \frac{\hat{k}_I}{\hat{c}_A},\\
g_N = \frac{\hat{g}_N}{\hat{c}_A}, \quad g_A = \frac{\hat{g}_A}{\hat{c}_A}, \quad g_S = \frac{\hat{g}_S}{\hat{c}_A}\\
r_T = \frac{\hat{c}_I\,\hat{r}_T\,\hat{A}_{\max}}{\hat{c}_A}, \quad d = \sqrt{\frac{\hat{d}_I}{\hat{d}_S}}.
\end{gathered} \tag{4}$$

We note that, due to the range of ecological feasibility for our parameters reported in Table 1, we assume $k_S > 0$, $k_N > 0$, $r_P \geq 0$, $k_A > 0$, $k_I > 0$, $g_N > 0$, $g_A > 0$, $r_T \geq 0$, and $d > 0$. Moreover, we assume that in the absence of seeds, seedlings and toxicity, the growth rate of adults is positive for all $\hat{A} > 0$, which implies

$$0 < k_A < 1. \tag{5}$$

Ecologically feasible ranges of the nondimensionalised parameters, based on the associated dimensional values in Table 1, can be found in Table 2.

Mathematical analysis: aims and goals. We determine the spatially homogeneous steady states (Section 3) and their linear stability with respect to spatially homogeneous and heterogeneous perturbations (Section 4). Furthermore, we investigate the presence of travelling waves (Section 5), determine properties of the wave profile, and determine the wave speed. To facilitate presentation, we organise the main results in Propositions and Theorems.

3. Spatially homogeneous steady states

For future reference and notational convenience, we introduce the establishment function

$$f(I) = \frac{1}{1+\gamma\,e^{r_T I}}. \tag{6}$$

Proposition 1. *System (3) admits two spatially homogeneous steady states,*

$$\mathcal{E}_0^* = (0,0,0,0) \tag{7}$$

and

$$\mathcal{E}_1^* = \left(\frac{A_*}{k_S},\ \frac{A_*(A_*+k_A-1)}{g_A g_N (1-A_*)},\ A_*,\ \frac{A_*}{k_I}\right). \tag{8}$$

Here, $A_* \in (1-k_A,\ 1)$ is the unique solution to

$$f\left(\frac{A}{k_I}\right) = \phi(A), \tag{9}$$

where

$$\phi(X) := -\frac{k_S\left(k_N + g_A\,(1-X) + \frac{r_P}{k_I}\,X\right)(1-k_A-X)}{g_A\,g_N\,g_S\,(1-X)}. \tag{10}$$

Proof. Spatially homogeneous steady states associated to system (3) are given by the solutions to

$$0 = A - k_S\,S, \tag{11a}$$

$$0 = g_S\,S\,f(I) - N\,\left(k_N + r_P\,I + g_A\,(1-A)\right), \tag{11b}$$

$$0 = A\,(1-k_A-A) + g_A\,g_N\,N\,(1-A), \tag{11c}$$

$$0 = A - k_I\,I. \tag{11d}$$

First, we observe that system (11) admits a trivial solution where all components vanish (representing bare soil):

$$\mathcal{E}_0^* = \left(S_0^*, N_0^*, A_0^*, I_0^*\right) = (0,0,0,0)\,. \tag{12}$$

In order to compute the nontrivial equilibria of System (3), we first solve Eq. (11a) and (11d) which lead to

$$S = \frac{A}{k_S}, \qquad I = \frac{A}{k_I}, \tag{13}$$

respectively. Substituting Eq. (13) into Eq. (11b) we obtain

$$\frac{g_S}{k_S}\,A\,f\left(\frac{A}{k_I}\right) = N\,\left(k_N + r_P\,I + g_A\,(1-A)\right). \tag{14}$$

Solving Eq. (14) for N we obtain

$$N = \frac{g_S\,f\left(\frac{A}{k_I}\right)}{k_S\left(k_N + \frac{r_P}{k_I}\,A + g_A\,(1-A)\right)}\,A. \tag{15}$$

Substituting Eq. (15) into Eq. (11c) yields

$$f\left(\frac{A}{k_I}\right)A = \phi(A)\,A. \tag{16}$$

Clearly, $A = 0$ is a solution to (16), leading to the trivial solution $\mathcal{E}_0^*$ (12); division by A leads to (9).

It remains to show that Eq. (9) has a unique nontrivial solution on the (ecologically feasible) interval $(0,1)$. We observe that for $X \in [0,1)$, the function $\phi(X)$ satisfies the following properties:

- $\phi(0) < 0$,
- $\lim_{X\to 1}\phi(X) = +\infty$ (g has a vertical asymptote at $X = 1$),
- $\phi''(X) > 0$ (ϕ is convex),
- $\phi(X) = 0$ if and only if $X = 1 - k_A$ (ϕ has a unique root in the interval $X \in (0,\ 1)$).

Furthermore, the establishment function $f(X)$ (6) satisfies the following properties:

- $f(0) = \frac{1}{1+\gamma} > 0$,
- $f'(X) < 0$ for all $X \in \mathbb{R}$ (f is strictly monotonically decreasing)
- $f(X) > 0$ for all $X \in \mathbb{R}$

Consequently, there exists a unique $A_* \in (0,1)$ that satisfies Eq. (9). Moreover, since $f(X)$ is positive and $\phi(X)$ is positive only if $X > 1-k_A$, we find that $A_* > 1 - k_A$; see also Fig. 2.

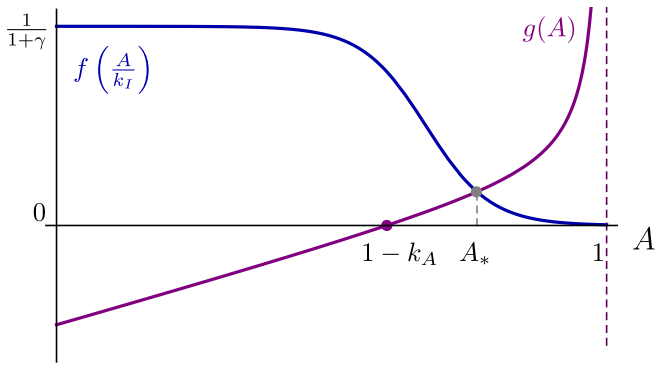

Fig. 2. Schematic representation of the functions $f\left(\frac{A}{k_I}\right)$ (blue solid line) and $\phi(A)$ (purple solid line) as defined in Eq. (6) and Eq. (10), respectively, for $\gamma = 10^{-5}$, $r_T = 48$, $k_S = 1.3$, $k_N = 0.08$, $g_A = 1$, $r_P = 0$, $k_I = 2.8$, $k_A = 0.4$, $g_N = 13$, and $g_S = 0.13$. The purple dot corresponds to the unique zero of $\phi(A)$ in the interval $A \in [0,\ 1]$, whereas the grey dot corresponds to the unique A_* where $f\left(\frac{A}{k_I}\right) = \phi(A)$, i.e. the A-component of the unique nontrivial steady state of System (3).

Therefore, we have that the unique nontrivial spatially homogeneous steady state of System (3) is given by

$$\begin{aligned}\mathcal{E}_1^* &= \left(S_1^*, N_1^*, A_1^*, I_1^*\right)\\ &= \left(\frac{A_*}{k_S},\ \frac{g_S\,f\left(\frac{A_*}{k_I}\right)}{k_S\left(k_N + \frac{r_P}{k_I}\,A_* + g_A\,(1-A_*)\right)}\,A_*,\ A_*,\ \frac{A_*}{k_I}\right).\end{aligned} \tag{17}$$

Using $f\left(\frac{A_*}{k_I}\right) = \phi(A_*)$ yields (8). □

For future reference, based on the results of Proposition 1, we write

$$A_* = 1 - \delta\,k_A, \quad 0 < \delta_{\min} < \delta < 1, \tag{18}$$

see also Fig. 2. The lower bound $\delta_{\min}$ can be determined by observing that the establishment function $f(I)$ is bounded above by $\frac{1}{1+\gamma}$ and hence $\phi(A_*) < \frac{1}{1+\gamma}$. Solving $\phi(1-\delta_{\min}k_A) = \frac{1}{1+\gamma}$ leads to

$$\delta_{\min} = \left(1 + \frac{1}{1+\gamma}\,\frac{\frac{g_A\,g_N\,g_S}{k_S}}{k_N + \frac{r_P}{k_I}}\right)^{-1} + \mathcal{O}(k_A). \tag{19}$$

Moreover, according to the parameter values reported in Table 2, we have $k_A = 0.04 \ll 1$. In the upcoming analysis, we will occasionally utilise the fact that k_A is small by employing k_A as a (regular) perturbation parameter, in order to gain insight into the solutions of complicated algebraic equations, by expanding these solutions in powers of k_A.

4. Linear stability

4.1. Spatially homogeneous perturbations

In this section, we analyse the linear stability of spatially homogeneous steady states $\mathcal{E}_0^*$ (7) and $\mathcal{E}_1^*$ (8) with respect to spatially homogeneous perturbations.

Proposition 2. *The trivial steady state $\mathcal{E}_0^*$ (7) is unstable with respect to spatially homogeneous perturbations. The nontrivial steady state $\mathcal{E}_1^*$ (8) is linearly stable with respect to spatially homogeneous perturbations, as long as*

$$\begin{aligned}-\frac{g_A\,g_N\,g_S}{k_S}\,f'\left(\frac{1}{k_I}\right) &< \frac{1}{k_A}\,\frac{1}{\delta^3}\left(k_N + k_I + \frac{r_P}{k_I}\right)(1+\delta k_I)\\ &\times\left(1 + \delta\left(k_N + \frac{r_P}{k_I}\right)\right) + \mathcal{O}(1)\,,\end{aligned} \tag{20}$$

assuming $0 < k_A \ll 1$.

Proof. The Jacobian matrix corresponding to System (3) reads

$$J = \begin{pmatrix} -k_S & 0 & 1 & 0 \\ g_S\, f(I) & -k_N - g_A\,(1-A) - r_P\, I & g_A\, N & g_S\, S\, f'(I) - r_P\, N \\ 0 & g_A\, g_N\,(1-A) & 1 - 2A - k_A - g_A\, g_N\, N & 0 \\ 0 & 0 & 1 & -k_I \end{pmatrix}. \tag{21}$$

The characteristic polynomial associated to J evaluated at $\mathcal{E}_0^*$ is given by

$$p_0(\lambda) = \left(-\lambda - k_I\right)\left(\lambda^3 + a_{02}\,\lambda^2 + a_{01}\,\lambda + a_{00}\right), \tag{22}$$

where

$$\begin{aligned} a_{02} &= -1 + g_A + k_S + k_A + k_N, \\ a_{01} &= k_S\,(g_A + k_N) - (1 - k_A)(g_A + k_N + k_S), \\ a_{00} &= -\frac{g_A\, g_N\, g_S}{1+\gamma} - k_S\,(g_A + k_N)(1 - k_A). \end{aligned} \tag{23}$$

The polynomial $p_0(\lambda)$ admits four roots λ_i^0, $i = 1, \dots, 4$. We identify $\lambda_1^0 = -k_I < 0$, whereas the sign of the other three eigenvalues is investigated using the Routh–Hurwitz criterion. In particular, $\mathcal{E}_0^*$ is asymptotically linearly stable if and only if the roots of the third order polynomial in (22) have negative real part, i.e. if and only if

$$a_{02},\, a_{00} > 0 \quad \text{and} \quad a_{02}\, a_{01} - a_{00} > 0. \tag{24}$$

Due to the non-negativity constraints on our parameters and the bound on k_A (5), we have $a_{00} < 0$, thereby violating the Routh–Hurwitz criterion. Consequently, at least one of the three eigenvalues $\lambda_{2,3,4}^0$ has positive real part, and the equilibrium $\mathcal{E}_0^*$ is unstable with respect to spatially homogeneous perturbations.

Concerning $\mathcal{E}_1^*$, we define two new parameters $\eta, \zeta > 0$ as

$$\eta := \frac{r_P}{k_I}, \qquad \zeta := -\frac{g_A\, g_N\, g_S}{k_S}\, f'\left(\frac{1}{k_I}\right). \tag{25}$$

As long as η, ζ and all parameters in System (11) are $\mathcal{O}(1)$ with respect to $k_A \ll 1$, the characteristic polynomial associated to J evaluated at $\mathcal{E}_1^*$ is given by

$$p_1(\lambda) = \left(k_S + \lambda\right)\left(k_I + \lambda\right)\left(k_N + \frac{r_P}{k_I} + \lambda\right)(1 + \delta\,\lambda) + \mathcal{O}(k_A). \tag{26}$$

Due to the non-negativity assumption on the model parameters, $p(\lambda)$ admits four negative roots, which in turn implies that $\mathcal{E}_1^*$ is a stable steady state w.r.t. homogeneous perturbations. The case where η and/or ζ are much larger than $\mathcal{O}(1)$ is analysed in Appendix. The outcome of this analysis is that all eigenvalues have negative real part as long as $\zeta < \frac{1}{k_A}\zeta_0^H + \mathcal{O}(1)$, with the Hopf bifurcation threshold ζ_0^H given by (A.3). Substituting η and ζ (25) yields (20). □

Corollary 1. *The nontrivial steady state $\mathcal{E}_1^*$ (8) is stable with respect to spatially homogeneous perturbations for the parameter ranges in Table 2.*

Proof. From (6), we see that $-f'\left(\frac{1}{k_I}\right) \to 0$ as $r_T \downarrow 0$. Moreover, $-f'\left(\frac{1}{k_I}\right) \approx \frac{r_T}{\gamma} e^{-\frac{r_T}{k_I}} \to 0$ as $r_T \to \infty$. The function $r_T \mapsto -f'\left(\frac{1}{k_I}\right)$ has a unique maximum, attained at $(r_T)_{\max} = k_I\left(-\log\gamma - \frac{2}{\log\gamma} + \mathcal{O}\left((\log\gamma)^{-3}\right)\right)$, with value $-f'\left(\frac{1}{k_I}\right)\Big|_{r_T=(r_T)_{\max}} = \frac{k_I}{4}\left(\log\gamma + \frac{1}{\log\gamma}\right) + \mathcal{O}\left((\log\gamma)^{-3}\right)$. Implementing the values of Table 2, we combine the above with $\frac{g_A g_N g_S}{k_S} < 4 \cdot 10^1$ to obtain

$$-\frac{g_A\, g_N\, g_S}{k_S}\, f'\left(\frac{1}{k_I}\right) < 3.2 \cdot 10^2.$$

From the same Table, we infer

$$\frac{1}{k_A}\frac{1}{\delta^3}\left(k_N + k_I + \frac{r_P}{k_I}\right)(1 + \delta k_I)\left(1 + \delta\left(k_N + \frac{r_P}{k_I}\right)\right) > 3.0 \cdot 10^2.$$

We see that straightforward estimates do not suffice to conclude that (20) is satisfied for the parameter ranges in Table 2; however, the bounds are sufficiently close to conclude that the region in parameter space for which $\mathcal{E}_1^*$ is unstable with respect to spatially homogeneous perturbations is relatively small. Furthermore, the value of δ is determined by the other system parameters through (9) and (18). Hence, we numerically determine the maximal real part of the eigenvalues of $\mathcal{E}_1^*$, by first determining the value of A_* (cf. Proposition 1) and then calculating the eigenvalues of the associated Jacobian. For the parameter ranges in Table 2, the maximum real part of the eigenvalues is found to be $-0.96 < 0$. Hence, $\mathcal{E}_1^*$ is stable with respect to spatially homogeneous perturbations for the parameter ranges in Table 2. □

4.2. Spatially heterogeneous perturbations

Since Turing patterns can emerge when steady states are stable with respect to spatially homogeneous perturbations but lose their stability when considering spatially heterogeneous perturbations, in this section we focus our attention only on the steady state $\mathcal{E}_1^*$ (see Section 4.1).

Proposition 3. *The spatially homogeneous steady state $\mathcal{E}_1^*$ (8) is linearly stable with respect to spatially heterogeneous perturbations, as long as*

$$\begin{aligned} -\frac{g_A\, g_N\, g_S}{k_S + h^2}\, f'\left(\frac{1}{k_I + h^2}\right) &< \frac{1}{k_A}\frac{1}{\delta^3}\left(k_N + k_I + h^2 + \frac{r_P}{k_I + h^2}\right) \\ &\times \left(1 + \delta(k_I + h^2)\right)\left(1 + \delta\left(k_N + \frac{r_P}{k_I + h^2}\right)\right) + \mathcal{O}(1), \end{aligned} \tag{27}$$

for all $h \in \mathbb{R}$, assuming $0 < k_A \ll 1$.

Proof. We introduce the following non-uniform perturbations:

$$\begin{aligned} S(t,x,y) &= S_1^* + \tilde{S}(0)\, e^{ikx + ily + \lambda t}, \\ N(t,x,y) &= N_1^* + \tilde{N}(0)\, e^{ikx + ily + \lambda t}, \\ A(t,x,y) &= A_1^* + \tilde{A}(0)\, e^{ikx + ily + \lambda t}, \\ I(t,x,y) &= I_1^* + \tilde{T}(0)\, e^{ikx + ily + \lambda t}, \end{aligned} \tag{28}$$

where the (spatial) wave number of the perturbation is defined as $h = \sqrt{k^2 + l^2}$ and λ represents the temporal growth. Linearising System (3) around $\mathcal{E}_1^*$, we obtain the following system for the perturbations $\tilde{S}$, $\tilde{N}$, $\tilde{A}$, $\tilde{T}$ defined in (28):

$$\begin{aligned} \lambda\tilde{S} &= \tilde{A} - \left(k_S + h^2\right)\tilde{S}, \\ \lambda\tilde{N} &= g_N\, f(I_1^*)\,\tilde{S} - \tilde{N}\left(g_A\,(1 - A_1^*) + k_N + r_P\, I_1^*\right) + g_A\, N_1^*\,\tilde{A} \\ &\quad + \tilde{T}\left(g_S\, S_1^*\, f'(I_1^*) - r_P\,\tilde{T}\right), \\ \lambda\tilde{A} &= \tilde{A}\left(1 - 2A_1^* - k_A - g_A\, g_N\, N_1^*\right) + g_A\, g_N\,\tilde{N}\left(1 - A_1^*\right), \\ \lambda\tilde{T} &= \tilde{A} - \left(k_I + d^2\, h^2\right)\tilde{T}. \end{aligned} \tag{29}$$

System (29) can be written as an eigenvalue problem $J_h\,\tilde{U} = \lambda\,\tilde{U}$, where $\tilde{U} = \left(\tilde{S}, \tilde{N}, \tilde{A}, \tilde{T}\right)$ and (see Eq. (30) in Box I).

We observe that this eigenvalue problem can be made identical to the eigenvalue problem for spatially homogeneous perturbations, as studied in the proof of Proposition 2, by replacing

$$k_S \to k_S + h^2, \quad k_I \to k_I + h^2. \tag{31}$$

Hence, the same stability criterion as in Proposition 2 applies, with the substitution (31). □

Corollary 2. *The nontrivial steady state $\mathcal{E}_1^*$ (8) cannot undergo a Turing bifurcation for the parameter ranges in Table 2.*

Proof. From the proof of Proposition 2, we see that $-f'(X)$ has a unique maximum at a fixed value of $\frac{r_T}{k_I}$ for γ fixed. The right hand side of (27) is by construction independent of r_T, since r_T only occurs in the derivative of f (encoded by ζ), and the right hand side of (27) is an expansion of a bound on ζ.

$$J_h = \begin{pmatrix} -k_S - h^2 & 0 & 1 & 0 \\ g_N\, f(I_1^*) & -g_A\,(1 - A_1^*) - k_N - r_P\, I_1^* & g_A\, N_1^* & g_S\, S_1^*\, f'(I_1^*) - r_P\, N_1^* \\ 0 & g_A\, g_N\,(1 - A_1^*) & 1 - 2A_1^* - k_A - g_A\, g_N\, N_1^* & 0 \\ 0 & 0 & 1 & -k_I - d^2\, h^2 \end{pmatrix}. \tag{30}$$

Box I.

From Proposition 2, we know that $\mathcal{E}_1^*$ is stable with respect to spatially homogeneous perturbations, which is equivalent to setting $h = 0$ in (27). We infer from Proposition 2 that (27) is satisfied for $h = 0$ for all admissible parameter ranges in Table 2. Therefore, for given k_I and γ, we may assume without loss of generality that r_T is chosen such that $-f'\left(\frac{1}{k_I}\right)$ is maximal, as $(r_T)_{\max} = 3.3 \cdot 10^1$ falls (well) within the admissible range of r_T. When $k_I \to k_I + h^2$ is increased, this argument continues to hold until r_T reaches its maximal admissible value; when h is increased beyond this point, $-f'\left(\frac{1}{k_I}\right)$ is smaller than its unique maximal value. Combining this argument with $\frac{g_A g_N g_S}{k_S + h^2} < \frac{g_A g_N g_S}{k_S}$, we see that

$$-\frac{g_A\, g_N\, g_S}{k_S + h^2}\, f'\left(\frac{1}{k_I + h^2}\right) \leq -\frac{g_A\, g_N\, g_S}{k_S}\, f'\left(\frac{1}{k_I}\right)$$

for all $h \in \mathbb{R}$.

The right hand side of (27) is non-monotonic in h. However, a lower bound is found analogously to the proof of Corollary 1 by setting $r_P = 0$ and minimising the other parameters. Since all components of the right hand side of (27) are increasing functions of h^2, the value of the right hand side of (27) is bounded from below by its value for $h = 0$. The above arguments imply that (27) therefore remains satisfied for $h > 0$.

We conclude that no Turing bifurcation can take place for the parameter ranges in Table 2. □

5. Travelling waves

As shown in Section 4, for the parameter ranges in Table 2, the nontrivial steady state $\mathcal{E}_1^*$ is spectrally stable (Corollary 1), whereas the trivial steady state $\mathcal{E}_0^*$ is unstable (Proposition 2). In order to investigate the existence of potential travelling waves solutions of System (1) from the numerical viewpoint, we hence focus our attention on a sufficiently large, one-dimensional domain with Neumann boundary conditions (mimicking the dynamics on an unbounded domain). With this setup, numerical simulations show the emergence of travelling wave solutions invading the unstable steady state $\mathcal{E}_0^*$ for a broad range of parameter values (see an example in Fig. 3). These simulations suggest the existence of a travelling wave with fixed wave speed in System (1) on an unbounded one-dimensional spatial domain. In this section, we investigate the existence of such a travelling wave, and provide arguments for its existence in a large part of parameter space. Moreover, we show that the numerically measured wave speed coincides with the so-called linear spreading speed, to a high degree of accuracy. This suggests that the numerically observed front can be classified as a *pulled front*, that is, where the linear spreading of small perturbations pulls the front into the linearly unstable bare soil steady state [35].

To prepare the analysis, we introduce a co-moving frame via the variable $\xi = x - c\,t$, where c represents the wave speed. System (3) hence becomes

$$S' = u, \tag{32a}$$

$$u' = -c\,u - A + k_S\, S, \tag{32b}$$

$$N' = -\frac{1}{c}\left(g_S\, S\, f(I) - N\,\left(k_N + r_P\, I + g_A\,(1 - A)\right)\right), \tag{32c}$$

$$A' = -\frac{1}{c}\left(A\,(1 - k_A - A) + g_A\, g_N\, N\,(1 - A)\right), \tag{32d}$$

$$I' = \frac{v}{d}, \tag{32e}$$

$$v' = \frac{1}{d}\left(-\frac{c}{d}\, v - A + k_I\, I\right), \tag{32f}$$

which can also be expressed in the compact form $z' = F(z)$, where $z = (S, u, N, A, I, v)$. Here we follow the common practice to scale both I and its derivative v with the square root of the scaled diffusivity d^2. However, note that all statements in this section would continue to hold if the choice $I' = v$ would have been made.

System (32) admits the two equilibria

$$z_0^* := (0, 0, 0, 0, 0, 0), \tag{33a}$$

$$z_1^* := \left(S_1^*, 0, N_1^*, A_1^*, I_1^*, 0\right), \tag{33b}$$

where the components of z_1^* coincide with those defined in Eq. (8). The equilibria z_0^* and z_1^* are the representation of the spatially homogeneous steady states $\mathcal{E}_0^*$ (7) and $\mathcal{E}_1^*$ (8) in the travelling wave framework.

In this context, a right-moving front (with $c > 0$) invading the trivial steady state $\mathcal{E}_0^*$ coincides with an heteroclinic connection from z_1^* to z_0^*. Such an orbit must therefore lie in the intersection of the unstable manifold of z_1^* (denoted by $\mathcal{W}^u(z_1^*)$) and the stable manifold of z_0^* (denoted by $\mathcal{W}^s(z_0^*)$). To investigate the potential existence of right-moving fronts we hence need to derive the parametric conditions such that

$$\mathcal{W}^u(z_1^*) \cap \mathcal{W}^s(z_0^*) \neq \emptyset, \tag{34}$$

which follow directly from the investigation of the dimensions of the stable and unstable manifolds of z_0^* and z_1^*.

The main point of our analysis consists in studying the characteristic polynomial associated to System (32), which can be expressed as

$$P(\lambda) = \det\left(\lambda\,\mathbb{I} - DF(z^*)\right). \tag{35}$$

The roots of $P(\lambda)$ evaluated at z_i^*, $i = 0, 1$ will provide information about the dimension of the stable and unstable manifolds of these equilibria, indicating whether Eq. (34) can hold.

5.1. Local analysis of z_0^*

Theorem 1. *The dimensions of the stable and unstable subspaces of z_0^* (denoted as $E^s(z_0^*)$ and $E^u(z_0^*)$, respectively) satisfy*

$$\dim\left(E^s(z_0^*)\right) = \dim\left(E^u(z_0^*)\right) = 3. \tag{36}$$

Proof. The characteristic polynomial of System (32) at z_0^* is given by

$$P_0(\lambda) = \frac{1}{c^2 d^2}\, \tilde{P}_1(\lambda)\, \tilde{P}_2(\lambda), \tag{37}$$

with

$$\tilde{P}_1(\lambda) := \lambda\,(c + d^2\,\lambda) - k_I \tag{38}$$

and

$$\tilde{P}_2(\lambda) := \frac{g_A\, g_N\, g_S}{1 + \gamma} + (1 - k_A + c\,\lambda)\,(g_A + k_N - c\,\lambda)\,(k_S - \lambda(c + \lambda)). \tag{39}$$

The quadratic function $\tilde{P}_1(\lambda)$ is convex and negative at $\lambda = 0$; therefore it admits two real roots of opposite sign, namely $\lambda_1^- < 0 < \lambda_1^+$. To study

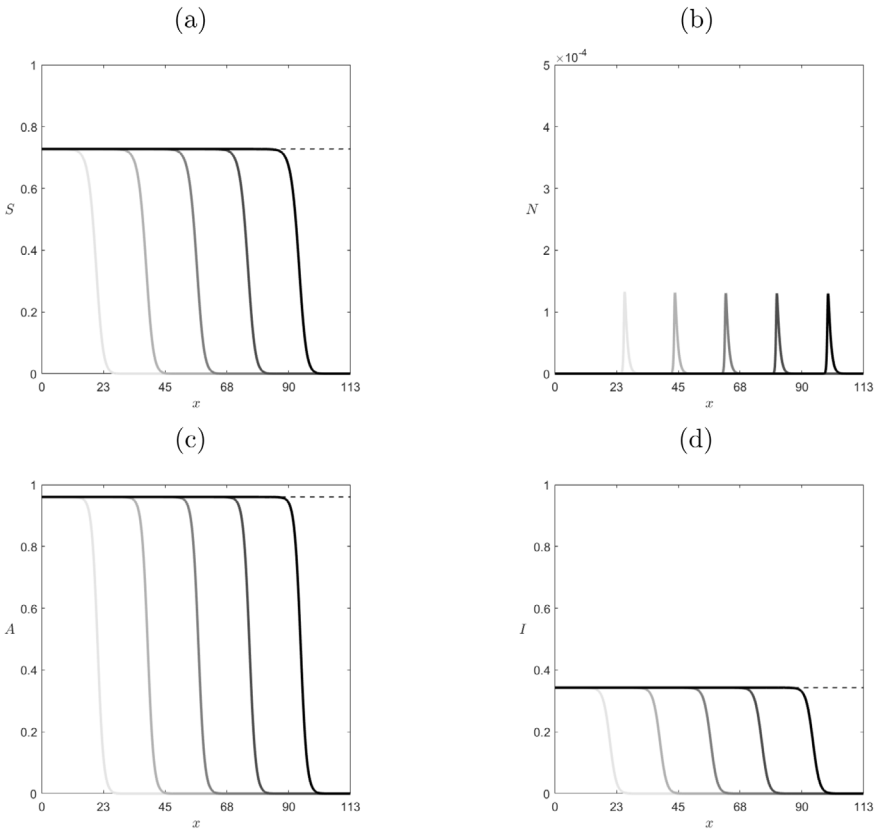

Fig. 3. Numerical profiles for (a) S, (b) N, (c) A, and (d) I obtained by simulating Eq. (3) for $t \in [0, 87.5]$. Profiles are shown a t distance $\Delta t = 17.5$ for $g_S = 0.132$, $k_S = 1.32$, $g_N = 20$, $r_T = 4080$, $k_N = 2$, $r_P = 480$, $g_A = 0.8$, $d = 0.913$, and other parameters values as in Table 2. The intensity of the shading (from light grey to black) increases with t. Note that for these parameter values, the value of N_1^* (17) is numerically indistinguishable from zero.

the roots of $\tilde{P}_2(\lambda)$, we write

$$\tilde{P}_2(\lambda) = c^2\lambda^4 + c\left(c^2-\alpha\right)\lambda^3 - \left(\beta + c^2 k_S + c^2\alpha\right)\lambda^2 + c\left(\alpha k_S - \beta\right)\lambda + \frac{g_A g_N g_S}{1+\beta} + \beta k_S, \tag{40}$$

where $\alpha = g_A + k_A + k_N - 1$ and $\beta = \left(g_A + k_N\right)\left(1 - k_A\right)$; note that $\beta > 0$.

The sign of the roots of $\tilde{P}_2(\lambda)$ can be investigated applying the Routh–Hurwitz criterion, by rewriting Eq. (40) as

$$\tilde{P}_2(\lambda) = c^2\left(\lambda^4 + a_3\lambda^3 + a_2\lambda^2 + a_1\lambda + a_0\right), \tag{41}$$

where

$$\begin{aligned} a_3 &= \frac{1}{c}\left(c^2-\alpha\right), \\ a_2 &= -\frac{1}{c^2}\left(\beta + c^2\alpha + c^2 k_S\right), \\ a_1 &= \frac{1}{c}\left(\alpha k_S - \beta\right), \\ a_0 &= \frac{1}{c^2}\left(\frac{g_A g_N g_S}{1+\beta} + \beta k_S\right). \end{aligned} \tag{42}$$

Applying Descartes' rule of signs, which states that the number of roots with negative (resp. positive) real part corresponds to the number of sign changes (resp. permanences) on the coefficients of $\tilde{P}_2(\lambda)$, and taking into account the fact that $a_0 > 0$, we observe that the conditions $a_3 > 0$, $a_2 > 0$, and $a_1 > 0$ cannot be verified simultaneously, i.e. there is at least one sign variation and one permanence. Hence, the fourth order polynomial $\tilde{P}_2(\lambda)$ admits at least one root with positive and one with negative real part, denoted by λ_2^+ and λ_2^-.

Moreover, there are no purely imaginary roots of $\tilde{P}_2(\lambda)$ since $\tilde{P}_2(i\omega)$ is a real polynomial if and only if $\omega = \pm\sqrt{\frac{a_1}{a_3}}$ and a_1, a_3 have the same sign only for $a_2 < 0$, which implies

$$\tilde{P}_2(i\omega) = c^2\left(\omega^4 - a_2\omega^2 + a_0\right) > 0.$$

Consequently, we have (considering $\tilde{P}_2(0) = c^2 a_0 \neq 0$) that the centre eigenspace $E^c(z_0^*) = \emptyset$, from which it follows that the phase space can be decomposed into the direct sum of the stable and unstable eigenspaces $E^s(z_0^*)$ and $E^u(z_0^*)$ respectively, i.e. $E^s(z_0^*) \oplus E^u(z_0^*) = \mathbb{R}^6$.

Besides the two roots with opposite real signs λ_2^+ and λ_2^- derived above, we need to check the sign of the other two roots of $\tilde{P}_2(\lambda)$, which we define as $\hat{\lambda}_2$ and $\tilde{\lambda}_2$. We analyse all possible scenarios:

- If $\lambda_2^+, \lambda_2^- \in \mathbb{C}$, then $\hat{\lambda}_2$ and $\tilde{\lambda}_2$ must be equal to the complex conjugates of $\lambda_2^\pm$, i.e. $\hat{\lambda}_2 = \overline{\lambda_2^+}$ and $\tilde{\lambda}_2 = \overline{\lambda_2^-}$.
- If $\lambda_2^+ \in \mathbb{R}$, then $\hat{\lambda}_2$ must be positive and real. This is due to the fact that $\tilde{P}_2(0) = c^2 a_0 > 0$ and $\tilde{P}_2(\lambda) \sim c^2\lambda^4$ as $\lambda \to \infty$; therefore, the graph of $\tilde{P}_2(\lambda)$ must have an even number of crossings with the positive horizontal axis.
- Analogously, if $\lambda_2^- \in \mathbb{R}$, then $\tilde{\lambda}_2$ must be negative and real. This is due to the fact that $\tilde{P}_2(0) = c^2 a_0 > 0$ and $\tilde{P}_2(\lambda) \sim c^2\lambda^4$ as $\lambda \to -\infty$; therefore, the graph of $\tilde{P}_2(\lambda)$ must have an even amount of crossings with the negative real axis.

To summarise, we conclude that $P_0(\lambda)$ admits a total of three eigenvalues with positive real part (namely λ_1^+, λ_2^+ and $\hat{\lambda}_2$), and three with negative real part (namely λ_1^-, λ_2^- and $\tilde{\lambda}_2$), which leads to the claim of the theorem. □

5.2. Local analysis of z_1^*

Theorem 2. *Assume $0 < k_A \ll 1$ is sufficiently small. For $c^2 < d^2\left(k_N + \eta + \frac{1}{\delta}\right)$, the dimensions of the stable and unstable eigenspace of z_1^* (corresponding to $E^s(z_1^*)$ and $E^u(z_1^*)$, respectively) satisfy $\dim\left(E^s(z_1^*)\right) = 2$ and $\dim\left(E^u(z_1^*)\right) = 4$. Only when $c^2 > d^2\left(k_N + \eta + \frac{1}{\delta}\right)$ there exists a*

$\mathcal{O}(k_A^{-1})$-value of $\zeta = \zeta_H$ such that, if $\zeta > \zeta_H$, $\dim\left(E^s(z_1^*)\right) = 4$ and $\dim\left(E^u(z_1^*)\right) = 2$.

Proof. The characteristic polynomial of System (32) at z_1^*, in agreement with Eq. (35), is defined as

$$P_1(\lambda) := \det\left(\lambda\,\mathbb{I} - DF(z_1^*)\right).$$

Our analysis is based on the observation made at the end of Section 3 that, since $k_A \ll 1$, we can treat k_A as an asymptotically small perturbation parameter to investigate the roots of complicated algebraic expressions such as (35).

We write $A_* = 1 - \delta\, k_A$ with $0 < \delta < 1$, cf. (18). Recalling the definition of η and ζ in (25), we expand $P_1(\lambda)$ for small k_A and consider the four regimes

I. $\eta, \zeta \in \mathcal{O}(1)$,
II. $\eta \gg 1$, $\zeta \in \mathcal{O}(1)$,
III. $\eta \in \mathcal{O}(1)$, $\zeta \gg 1$,
IV. $\eta, \zeta \gg 1$.

Regime I: $\eta, \zeta \in \mathcal{O}(1)$. In this regime, the characteristic polynomial can be expressed as

$$P_1^I(\lambda) := \frac{1}{c^2 d^2}\left(\tilde{P}_1(\lambda)\,\tilde{Q}_1(\lambda)\left(c\,\lambda - \frac{1}{\delta}\right)\left(c\,\lambda - k_N - \eta\right)\right) + \mathcal{O}(k_A), \tag{43}$$

where

$$\tilde{Q}_1(\lambda) := \lambda\,(c + \lambda) - k_S \tag{44}$$

and $\tilde{P}_1(\lambda)$ as defined in (38). In the proof of Theorem 2, it is shown that the roots of $\tilde{P}_1(\lambda)$ are real and have opposite sign, i.e. $\lambda_1^- < 0 < \lambda_1^+$. The same statement holds for the roots of $\tilde{Q}_1(\lambda)$, since $\tilde{Q}_1(\lambda)$ is convex and $\tilde{Q}_1(0) = -k_S < 0$; we denote the roots of $\tilde{Q}_1(\lambda)$ as $\mu_1^- < 0 < \mu_1^+$. The two remaining roots of the leading order expression of $P_1^I(\lambda)$ (43) are given by $\frac{1}{c\,\delta}$ and $\frac{k_N+\eta}{c}$, which are both real and positive. All roots of the leading order expression of $P_1^I(\lambda)$ are nondegenerate and bounded away from zero, and therefore perturb regularly for $k_A \ll 1$. Therefore, $\dim\left(E^s(z_1^*)\right) = 2$ and $\dim\left(E^u(z_1^*)\right) = 4$.

Regime II: $\eta \gg 1$, $\zeta \in \mathcal{O}(1)$. The $\mathcal{O}(k_A)$ terms in the expansion of P_1^I (43) do not depend on η. Hence, the roots of P_1 in regime II are equal to those in regime I. The only difference is that now the eigenvalue $\frac{k_N+\eta}{c} = \frac{\eta}{c} + \mathcal{O}(1)$, but this does not affect its sign, which remains positive. Therefore, as in Regime I, we obtain $\dim\left(E^s(z_1^*)\right) = 2$ and $\dim\left(E^u(z_1^*)\right) = 4$.

Regime III: $\eta \in \mathcal{O}(1)$, $\zeta \gg 1$. In this regime, the characteristic polynomial is to leading order given by

$$P_1^{III}(\lambda) := \frac{\tilde{Q}_1(\lambda)}{c^2 d^2}\left(\tilde{Q}_2(\lambda) - \delta\,\zeta\,k_A\right) + \mathcal{O}(k_A)\,\mathcal{O}(\zeta^0), \tag{45}$$

where

$$\tilde{Q}_2(\lambda) := \tilde{P}_1(\lambda)\left(c\,\lambda - \frac{1}{\delta}\right)\left(c\,\lambda - k_N - \eta\right) \tag{46}$$

and $\tilde{Q}_1(\lambda)$ as defined in (44). We therefore need to split our investigation into further subcases depending on the magnitude of $\zeta\,k_A$.

(i) $\zeta\,k_A \ll 1$: here $P_1^{III}(\lambda)$ is a regular perturbation of $P_1^I(\lambda)$; we obtain same result on the sign of the eigenvalues, that is, $\dim\left(E^s(z_1^*)\right) = 2$ and $\dim\left(E^u(z_1^*)\right) = 4$.

(ii) $\zeta\,k_A = \mathcal{O}(1)$: we write $\zeta = \frac{\zeta_1}{k_A}$ with $\zeta_1 \geq 0$. Substituting this assumption into Eq. (45) leads to

$$P_1^{III}(\lambda) = \frac{\tilde{Q}_1(\lambda)}{c^2 d^2}\left(\tilde{Q}_2(\lambda) - \delta\,\zeta_1\right) + \mathcal{O}(k_A). \tag{47}$$

When $\zeta_1 = 0$, we have that $P_1^{III}(\lambda) = P_1^I(\lambda)$, hence the sign of the eigenvalues is identical. When $\zeta_1 > 0$, since $\tilde{Q}_2(0) = -\frac{k_I\,(k_N+\eta)}{\delta} < 0$ and $\tilde{Q}_2(\lambda) \sim c^2 d^2 \lambda^4$ as $\lambda \to \pm\infty$, we have that $\tilde{Q}_2(\lambda) - \delta\,\zeta_1$ must admit at least one positive and one negative real root. For ζ_1 sufficiently small, the roots of $P_1^{III}(\lambda)$ are a regular perturbation of the roots of $P_1^I(\lambda)$, which implies that the two remaining roots of $\tilde{Q}_2(\lambda)$ are real and positive. As ζ_1 is increased, this root pair undergoes a (stabilising) Hopf bifurcation for sufficiently large values of ζ_1, namely for $\zeta_1 = \zeta_1^H$ where

$$\zeta_1^H = \frac{(\delta\,\eta + \delta\,k_N + 1)\left(d^2 - c^2\delta\,(\delta\,k_I + 1)\right)\left(d^2\,(\eta + k_N)^2 - c^2\,(\eta + k_N + k_I)\right)}{\delta^2\left(c^2\delta - d^2\,(\delta\,\eta + \delta\,k_N + 1)\right)^2}. \tag{48}$$

In other words, the real part of the complex conjugate roots of $\tilde{Q}_2(\lambda) - \delta\,\zeta_1$ is positive for $\zeta_1 < \zeta_1^H$, vanishes for $\zeta_1 = \zeta_1^H$, and is negative for $\zeta_1 > \zeta_1^H$. The expression for ζ_1^H in (48) is derived by solving $\tilde{Q}_2(i\,\omega) - \delta\,\zeta_1 = 0$ and imposing that the imaginary part of the resulting polynomial is zero. This gives an expression for ω which can be substituted back into $\tilde{Q}_2(i\,\omega) - \delta\,\zeta_1 = 0$; then we can subsequently solve this equation for ζ_1 to obtain ζ_1^H. Imposing the feasibility conditions $\omega^2 > 0$ and $\zeta_1 > 0$ we obtain that a Hopf bifurcation occurs if and only if

$$c > d, \quad 0 < \eta < \frac{c^2}{d^2} - 1, \quad 0 < k_N < \frac{c^2}{d^2} - 1 - \eta, \quad \frac{1}{\frac{c^2}{d^2} - k_N - \eta} < \delta < 1. \tag{49}$$

In particular, the above conditions hold if and only if $c^2 - d^2\left(k_N + \eta + \frac{1}{\delta}\right) > 0$.

(iii) $\zeta\,k_A \gg 1$: In this case, the equation $\tilde{Q}_2(\lambda) - \delta\,\zeta\,k_A = 0$ implies that $|\lambda| \gg 1$. To leading order, we thus have

$$c^2 d^2 \lambda^4 = \delta\,\zeta\,k_A, \tag{50}$$

which is solved by two real and two purely complex roots, namely

$$\lambda = \pm\left(\frac{\delta\,\zeta\,k_A}{c^2 d^2}\right)^{1/4}, \quad \lambda = \pm\,i\left(\frac{\delta\,\zeta\,k_A}{c^2 d^2}\right)^{1/4}.$$

Since the complex roots are purely imaginary to leading order, these need further unfolding to determine the sign of their real part. Including higher order terms ($\mathcal{O}(\lambda^3)$ and $\mathcal{O}(k_A^2)$, respectively) in Eq. (50) leads to the following refinement of the complex roots

$$\lambda = \frac{-c^2\delta + d^2\left(1 + \delta(k_N + \eta)\right)}{4\,c\,d^2\delta} \pm i\left(\frac{\delta\,\zeta\,k_A}{c^2 d^2}\right)^{1/4}\left(1 - k_A\right)^{1/4}. \tag{51}$$

We have two possibilities:

- If $c^2 - d^2\left(k_N + \eta + \frac{1}{\delta}\right) < 0$, the real part of the roots in (51) is positive. Therefore, taking into account the sign of the other roots of $P_{III}(\lambda)$, we find $\dim\left(E^s(z_1^*)\right) = 2$ and $\dim\left(E^u(z_1^*)\right) = 4$.
- If $c^2 - d^2\left(k_N + \eta + \frac{1}{\delta}\right) > 0$, the real part of the roots in (51) is negative, and we find $\dim\left(E^s(z_1^*)\right) = 4$ and $\dim\left(E^u(z_1^*)\right) = 2$. Note that, comparing to the case $\zeta k_A \ll 1$, this implies that somewhere between $\zeta k_A \ll 1$ and $\zeta k_A \gg 1$, a sign change must have occurred. This is precisely the Hopf bifurcation found at $\zeta k_A = \mathcal{O}(1)$, to wit, at $\zeta = \frac{\zeta_0^H}{k_A}$ (48).

Regime IV: $\eta, \zeta \gg 1$. To leading order, the characteristic polynomial in this regime coincides with the one in Regime III, i.e.

$$P_1^{IV}(\lambda) := \frac{\tilde{Q}_1(\lambda)}{c^2 d^2}\left(\tilde{Q}_2(\lambda) - \delta\,\zeta\,k_A\right) + \mathcal{O}(k_A)\,\mathcal{O}(\zeta^0) + \mathcal{O}(k_A)\,\mathcal{O}(\eta). \tag{52}$$

As in Regime III, we need to consider different relations between the orders of η and $\zeta\,k_A$ to determine the roots of $P_1^{IV}(\lambda)$.

(i) $\eta \gg \zeta\, k_A$: In this case, $P_1^{IV}(\lambda)$ is a regular perturbation of $P_1^I(\lambda)$; its roots are then given by $\lambda_1^{\pm}$, $\mu_1^{\pm}$, $\frac{1}{c\,\delta}$, and $\frac{\eta}{c} + \mathcal{O}(1)$.

(ii) $\eta \sim \zeta\, k_A$: Here we can express $\zeta = \zeta_1 \frac{\eta}{k_A}$, with $\zeta_0 = \mathcal{O}(1)$. To leading order, we obtain

$$P_1^{IV}(\lambda) := \frac{\tilde{Q}_1(\lambda)}{c^2 d^2}\left(\tilde{Q}_2(\lambda) - \delta\,\zeta_1\,\eta\right) + \mathcal{O}(k_A)\,\mathcal{O}(\eta). \tag{53}$$

The roots of (53) are studied by distinguishing two regimes. Focusing on $|\lambda| \gg 1$; in this case, $P_1^{IV}(\lambda) \sim \lambda^6 - \frac{\eta}{c}\lambda^5$, we obtain that one root is, to leading order, given by $\frac{\eta}{c}$. The other five roots are studied by investigating $P_1^{IV}(\lambda)$ to leading order in η for $\lambda = \mathcal{O}(1)$, i.e.

$$P_1^{IV}(\lambda) = -\frac{\tilde{Q}_1(\lambda)}{c^2 d^2}\left(\tilde{Q}_3(\lambda) + \delta\,\zeta_1\right)\eta + \mathcal{O}(k_A)\,\mathcal{O}(\eta), \tag{54}$$

where

$$\tilde{Q}_3(\lambda) := \tilde{P}_1(\lambda)\left(c\,\lambda - \frac{1}{\delta}\right). \tag{55}$$

Two roots are to leading order given by the roots of $\tilde{Q}_1(\lambda)$. For the other three, we see that, since $\tilde{Q}_3(0) = \frac{k_I}{\delta} > 0$ and $\tilde{Q}_3(\lambda) \sim c\,d^2\lambda^3$ as $\lambda \to \pm\infty$, the polynomial $\tilde{Q}_3(\lambda) + \delta\,\zeta_1$ always admits at least one negative real root. As for the other two, we observe that no Hopf bifurcation occurs in this case (since the only solution to $\tilde{Q}_3(i\,\omega) + \delta\,\zeta_1 = 0$ is given by $\omega = 0$). The sign of their real part hence remains the same as ζ_1 is varied, and since we know that for $\zeta_1 = 0$ the other two roots of $\tilde{Q}_3(i\,\omega) + \delta\,\zeta_1$ are real and positive, they remain positive for all ζ_1.

(iii) $\eta \ll \zeta\, k_A$: In this case, the characteristic polynomial is given by

$$P_1^{IV}(\lambda) := -\frac{\tilde{Q}_1(\lambda)}{c^2 d^2}\left(\tilde{Q}_3(\lambda)\,\eta + \delta\,\zeta\,k_A\right) + \mathcal{O}(k_A)\,\mathcal{O}(\eta). \tag{56}$$

Two roots are to leading order given by the roots of $\tilde{Q}_1(\lambda)$. Solving $\tilde{Q}_3(\lambda)\,\eta + \delta\,\zeta\,k_A = 0$ hence requires $|\lambda| \gg 1$. Expanding for large λ yields

$$\tilde{Q}_3(\lambda)\,\eta + \delta\,\zeta\,k_A = c^2\,d^2\lambda^4 - \eta\,c\,d^2\lambda^3 - \delta\,\zeta\,k_A + \mathcal{O}(\lambda^2). \tag{57}$$

Note that, as $-\delta\,\zeta\,k_A < 0$ and $c^2\,d^2\lambda^4 - \eta\,c\,d^2\lambda^3 - \delta\,\zeta\,k_A \sim c^2 d^2\lambda^4$ as $\lambda \to \pm\infty$, the leading order polynomial (57) has at least two real roots of opposite sign. To further determine the roots of (57), we consider four possible balances:

- If $c^2\,d^2\lambda^4 \sim \eta\,c\,d^2\lambda^3 \gg \delta\,\zeta\,k_A$, Eq. (57) reduces to leading order to $c^2\,d^2\lambda^4 - \eta\,c\,d^2\lambda^3 = 0$; this equation admits one real positive root $\lambda = \frac{\eta}{c}$ and one zero root with multiplicity three, that needs further unfolding. For $\lambda \sim 0$, Eq. (57) admits the three roots

$$\nu_1 = -\left(\frac{\delta\,\zeta\,k_A}{c\,d^2\eta}\right)^{1/3}, \quad \nu_2 = (-1)^{1/3}\left(\frac{\delta\,\zeta\,k_A}{c\,d^2\eta}\right)^{1/3}, \quad \nu_3 = (-1)^{2/3}\left(\frac{\delta\,\zeta\,k_A}{c\,d^2\eta}\right)^{1/3}. \tag{58}$$

  The roots ν_1 and ν_3 have negative real part, whereas ν_2 has positive real part.
- If $\eta\,c\,d^2\lambda^3 \sim \delta\,\zeta\,k_A \gg c^2\,d^2\lambda^4$, to leading order Eq. (57) admits the roots in (58), whose sign has been analysed in the previous balance point. The fourth root of (57) is real and negative.
- If $c^2\,d^2\lambda^4 \sim \delta\,\zeta\,k_A \gg \eta\,c\,d^2\lambda^3$, we have two real and two purely complex roots, namely

$$\lambda = \pm\left(\frac{\delta\,\zeta\,k_A}{c^2 d^2}\right)^{1/4}, \quad \lambda = \pm i\left(\frac{\delta\,\zeta\,k_A}{c^2 d^2}\right)^{1/4}.$$

  The sign of the real part of the complex roots is obtained by considering the higher order term $\eta\,c\,d^2\lambda^3$, from which we get

$$\lambda = \frac{\eta}{4\,c} \pm i\left(\frac{\delta\,\zeta\,k_A}{c^2 d^2}\right)^{1/4}.$$

  In this case we hence have one root with negative real part and three roots with positive real part.
- If $c^2\,d^2\lambda^4 \sim \eta\,c\,d^2\lambda^3 \sim \delta\,\zeta\,k_A$, we can define $\lambda := \lambda_0\,\eta$ and $\zeta\,k_A := \zeta_2\,\eta^4$. Eq. (57) thus becomes

$$\tilde{Q}_4(\lambda) - \delta\,\zeta_0 = 0, \tag{59}$$

  where $\tilde{Q}_4(\lambda) := c^2\,d^2\lambda_0^4 - c\,d^2\lambda_0^3$. This function satisfies $\tilde{Q}_4(0) = 0$ and $\tilde{Q}_4(\lambda) \to \infty$ as $\lambda \to \pm\infty$, therefore Eq. (59) admits two real roots of opposite sign for any $\zeta_2 > 0$. The two other complex roots have positive real part equal to $(-1)^{1/3}\left(\frac{\delta\,\zeta_2}{c\,d^2}\right)^{1/3}$ to leading order; since no Hopf bifurcations are possible, the sign of the real part of the complex roots remains positive for any $\zeta_2 > 0$. Hence also in this case we have one root with negative real part and three roots with positive real part.

Consequently, considering all possible balances we find for Regime IV that $\dim\left(E^s(z_1^*)\right) = 2$ and $\dim\left(E^u(z_1^*)\right) = 4$.

Conclusion. We observe that $c^2 < d^2\left(k_N + \eta + \frac{1}{\delta}\right)$ is automatically satisfied when $\eta \ll 1$, that is, in Regime II and Regime IV. Combining the results from Regimes I–IV, we see that $\dim\left(E^s(z_1^*)\right) = 2$ and $\dim\left(E^u(z_1^*)\right) = 4$ when $c^2 < d^2\left(k_N + \eta + \frac{1}{\delta}\right)$. Only when $c^2 - d^2\left(k_N + \eta + \frac{1}{\delta}\right) > 0$ there exists a $\mathcal{O}(k_A^{-1})$-value of $\zeta = \zeta_H$ such that, if $\zeta > \zeta_H$, $\dim\left(E^s(z_1^*)\right) = 4$ and $\dim\left(E^u(z_1^*)\right) = 2$. □

5.3. Existence of a travelling wave

In phase space, a travelling wave solution corresponds to a heteroclinic orbit connecting z_0^* and z_1^*, thus lying in the intersection of the unstable manifold of one equilibrium and the stable manifold of the other. We use the Local Stable Manifold Theorem to infer from Theorem 1 that the dimensions of the stable and unstable manifolds of z_0^* are

$$\dim\left(\mathcal{W}^s(z_0^*)\right) = \dim\left(\mathcal{W}^u(z_0^*)\right) = 3.$$

Likewise, we infer from Theorem 2 that the dimensions of the stable and unstable manifolds of z_1^* are either

$$\dim\left(\mathcal{W}^s(z_1^*)\right) = 2, \qquad \dim\left(\mathcal{W}^u(z_1^*)\right) = 4,$$

provided $c^2 < d^2\left(k_N + \eta + \frac{1}{\delta}\right)$, or

$$\dim\left(\mathcal{W}^s(z_1^*)\right) = 4, \qquad \dim\left(\mathcal{W}^u(z_1^*)\right) = 2,$$

provided $c^2 > d^2\left(k_N + \eta + \frac{1}{\delta}\right)$ and ζ (25) is sufficiently large, in particular $\zeta > \frac{\zeta_1^H}{k_A} + \mathcal{O}(1)$ (48).

Recall that the aim of this section is to obtain analytical insight into numerically observed travelling fronts that invade the trivial steady state, which for a right-moving front with positive speed c corresponds to a heteroclinic connection *from* z_1^* *to* z_0^*. Therefore, we take $c^2 < d^2\left(k_N + \eta + \frac{1}{\delta}\right)$, for reasons to be explained momentarily. Observing that $\operatorname{codim}\left(\mathcal{W}^u(z_0^*) \cap \mathcal{W}^s(z_1^*)\right) = 7$, whereas $\operatorname{codim}\left(\mathcal{W}^u(z_1^*) \cap \mathcal{W}^s(z_0^*)\right) = 5$, and taking into account the fact that the phase space is six-dimensional, we conclude that generically $\mathcal{W}^u(z_0^*) \cap \mathcal{W}^s(z_1^*) = \emptyset$ and $\dim\left(\mathcal{W}^u(z_1^*) \cap \mathcal{W}^s(z_0^*)\right) = 1$ (if non-empty). In the latter case, this intersection is generically transversal and hence persists when c is perturbed. This leads us to the following Corollary:

Corollary 3. *We generically expect a one-parameter family of heteroclinic connections from z_1^* to z_0^*, parametrised by the wave speed c, with $c^2 < d^2\left(k_N + \eta + \frac{1}{\delta}\right)$. Moreover, we expect this family to exist in an open region of parameter space. Every member of this family corresponds to a right-moving front invading the trivial steady state $\mathcal{E}_0^*$ (7).*

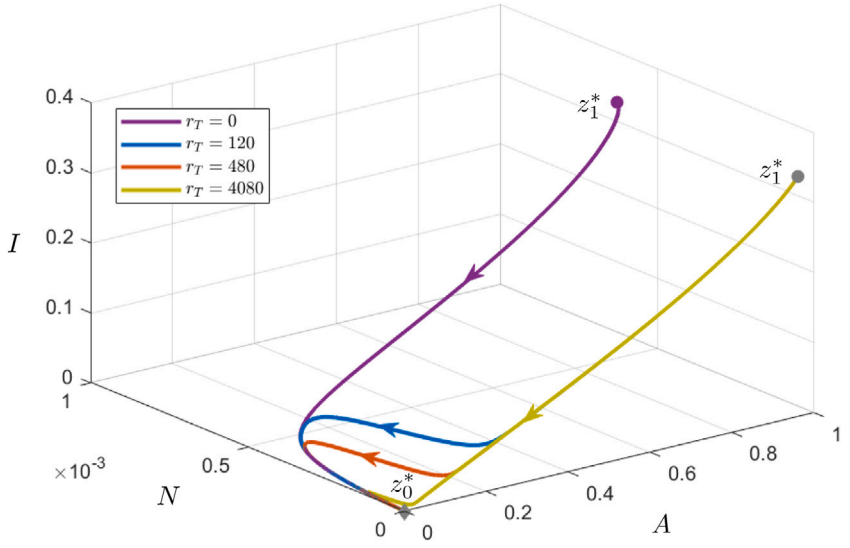

Fig. 4. Heteroclinic orbits connecting z_1^* (circle) to z_0^* (diamond) corresponding to the numerical travelling wave solution described in Fig. 3 in (A, N, I)-space for different values of r_T. Together with the ones fixed in Table 2, the parameter values are $g_S = 0.132$, $k_S = 1.32$, $g_N = 20$, $k_N = 2$, $r_P = 480$, $g_A = 0.8$, $d = 0.913$, and r_T as in the legend.

Note that the above arguments do not constitute a proof of the existence of a heteroclinic connection from z_1^* to z_0^*, as the intersection $\mathcal{W}^u(z_1^*) \cap \mathcal{W}^s(z_0^*)$ might be empty. However, in the upcoming section, we identify a parameter range for which such a heteroclinic connection exists (Theorem 3).

Remark 1. The same reasoning can be applied to generically expect the existence of a heteroclinic connection from z_0^* to z_1^*, for sufficiently large wave speeds $c > d\sqrt{k_N + \eta + \frac{1}{\delta}}$ and sufficiently large values of ζ. However, for all $c > d\sqrt{k_N + \eta + \frac{1}{\delta}}$, we have that $\zeta_1^H > \zeta_0^H$ (A.3), and ζ does not exceed ζ_0^H for the parameter ranges in Table 2, cf. Corollary 1. For this reason, we do not investigate this anomalous wave any further in the current paper.

The analytical investigation carried out above is confirmed by plotting the numerical solution shown in Fig. 3 in the (A, N, I)-space; this in fact reveals the presence of the predicted heteroclinic connection from z_1^* to z_0^* (see Fig. 4).

5.4. Properties of the wave profile

In this section, we derive generic properties satisfied by a right-moving travelling front solution to System (3), which is equivalent to a heteroclinic connection from z_1^* to z_0^* in System (32). These properties can be used to explore the connection between such a travelling wave and the Janzen–Connell distribution.

Lemma 1 (*Monotonicity of S and I*). *Let $(S(\xi), u(\xi), N(\xi), A(\xi), I(\xi), v(\xi))$ be a solution to System (32) representing a right-moving front travelling with speed $c > 0$. If $A'(\xi) < 0$ for all ξ, then $S'(\xi) < 0$ and $I'(\xi) < 0$ for all ξ.*

Proof. We first consider $S'(\xi)$. The proof strategy is based on deriving an explicit solution for $S(\xi)$ by means of a Green's function, which in turn allows us to obtain an explicit solution for $S'(\xi)$ as a function of $A'(\xi)$ using integration by parts.

We write Eqs. (32a)–(32b) as a single second order equation for S, yielding

$$S'' + c\,S' + A - k_S\,S = 0.$$

The boundary conditions

$$\lim_{\xi\to-\infty} S(\xi) = S_1^*, \qquad \lim_{\xi\to+\infty} S(\xi) = 0,$$

uniquely determine the solution

$$S(\xi) = e^{\mu_1^-\xi}\int_{-\infty}^{\xi} A(\zeta)\,\frac{e^{-\mu_1^-\zeta}}{\mu_1^+ - \mu_1^-}\,\mathrm{d}\zeta + e^{\mu_1^+\xi}\int_{\xi}^{+\infty} A(\zeta)\,\frac{e^{-\mu_1^+\zeta}}{\mu_1^+ - \mu_1^-}\,\mathrm{d}\zeta, \tag{60}$$

with

$$\mu_1^{\pm} = \frac{1}{2}\left(-c \pm \sqrt{c^2 + 4\,k_S}\right) \tag{61}$$

the roots of $\tilde{Q}_1(\lambda)$ (44). Consequently, we have that

$$\begin{aligned} S'(\xi) &= \mu_1^-\,e^{\mu_1^-\xi}\int_{-\infty}^{\xi} A(\zeta)\,\frac{e^{-\mu_1^-\zeta}}{\mu_1^+ - \mu_1^-}\,\mathrm{d}\zeta + \mu_1^+\,e^{\mu_1^+\xi}\int_{\xi}^{\infty} A(\zeta)\,\frac{e^{-\mu_1^+\zeta}}{\mu_1^+ - \mu_1^-}\,\mathrm{d}\zeta \\ &= -\,e^{\mu_1^-\xi}\left[A(\zeta)\,\frac{e^{-\mu_1^-\zeta}}{\mu_1^+ - \mu_1^-}\right]_{-\infty}^{\xi} + e^{\mu_1^-\xi}\int_{-\infty}^{\xi} A'(\zeta)\,\frac{e^{-\mu_1^-\zeta}}{\mu_1^+ - \mu_1^-}\,\mathrm{d}\zeta \\ &\quad -\,e^{\mu_1^+\xi}\left[A(\zeta)\,\frac{e^{-\mu_1^-\zeta}}{\mu_1^+ - \mu_1^-}\right]_{\xi}^{\infty} + e^{\mu_1^+\xi}\int_{\xi}^{\infty} A'(\zeta)\,\frac{e^{-\mu_1^+\zeta}}{\mu_1^+ - \mu_1^-}\,\mathrm{d}\zeta \\ &= e^{\mu_1^-\xi}\int_{-\infty}^{\xi} A'(\zeta)\,\frac{e^{-\mu_1^-\zeta}}{\mu_1^+ - \mu_1^-}\,\mathrm{d}\zeta + e^{\mu_1^+\xi}\int_{\xi}^{\infty} A'(\zeta)\,\frac{e^{-\mu_1^+\zeta}}{\mu_1^+ - \mu_1^-}\,\mathrm{d}\zeta, \end{aligned} \tag{62}$$

which is negative if $A'(\xi) < 0$ for all $\xi \in \mathbb{R}$. The proof of $I'(\xi) < 0$ is analogous, with $\lambda_1^{\pm}$, the roots of $\tilde{P}_1(\lambda)$ (38), replacing $\mu_1^{\pm}$. □

Lemma 2 (*Monotonicity of A*). *Let $(S(\xi), u(\xi), N(\xi), A(\xi), I(\xi), v(\xi))$ be a solution to System (32) representing a right-moving front travelling with speed $c > 0$. Then $A(\xi) < 1$ for all ξ. Moreover, there exists a $\xi_0 \in \mathbb{R}$ such that*

- *$A(\xi) > 1 - k_A$ for all $\xi < \xi_0$, and*
- *$A(\xi) < 1 - k_A$ and $A'(\xi) < 0$ for all $\xi \geq \xi_0$.*

Proof. From Eq. (32d) together with the positivity assumptions on N and the parameters g_A, g_N, it follows that when $A \geq 1$, then $A' > 0$. Therefore, if solution crosses the threshold $A = 1$ for a certain $\xi = \xi_1$, it will remain above $A = 1$ for all $\xi > \xi_1$. This contradicts the assumption on the travelling wave solution, that $A(\xi) \to 0$ as $\xi \to \infty$.

Again from Eq. (32d) together with the positivity assumptions on N and the parameters g_A, g_N, it follows that when $A \leq 1 - k_A$, then $A' < 0$. Therefore, if solution crosses the threshold $A = 1 - k_A$ for a certain $\xi = \xi_0$, it will remain below $A = 1 - k_A$ for all $\xi > \xi_0$. Since the travelling wave solution has $A(\xi) \to 0$ as $\xi \to \infty$ and $A(\xi) \to A_* > 1 - k_A$

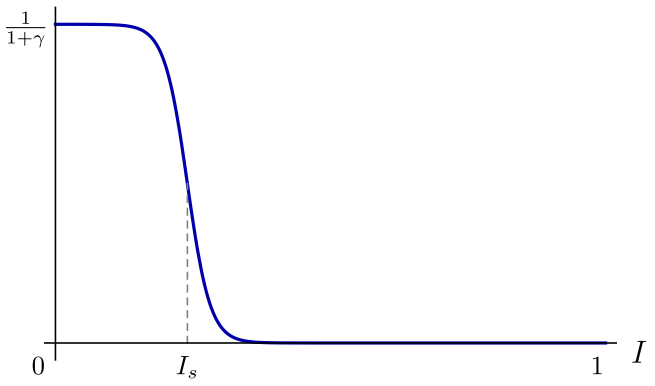

Fig. 5. Schematic representation of the establishment function $f(I)$ as defined in Eq. (6), for large values of r_T.

as $\xi \to -\infty$, it follows that the solution crosses the threshold $1-k_A$ for some ξ_0. Once the solution has crossed this threshold, it will continue to decrease (strictly monotonically) to zero. □

Remark 2. When $1-k_A < A < 1$, no monotonicity of A is generically guaranteed. By redefining $A = 1-k_A\,a$ and linearising System (32) around the nontrivial equilibrium A_* (corresponding to $a=\delta$), we have seen in Section 5.2 that in our travelling wave framework there are four unstable eigenvalues, hence leading to four associated eigenvectors with a nonzero a-component as follows:

$$a(\xi) = \delta + h_1\, e^{\frac{1}{c\delta}\xi} + h_2\, e^{\frac{k_N+\eta}{c}\xi} + h_3\, e^{\lambda_1^+\xi} + h_4\, e^{\mu_1^+\xi}.$$

Therefore, depending on the signs of the constants h_i, $i=1,\dots,4$, A can admit several local minima and maxima in a neighbourhood of A_*.

Lemma's 1 and 2 provide information on the monotonicity of S, I and A. However, for the seedling component N, one cannot derive monotonicity properties in full generality, due to the nature of the nonlinearity of Eq. (32c).

To mitigate this problem, we consider the establishment function $f(I)$ (6) for large values of r_T. We observe that, for sufficiently large r_T, $f(I)$ behaves like a switch function (see also Fig. 5):

$$f(I) \approx \begin{cases} \frac{1}{1+\gamma} & \text{if } r_T > 0,\ I \le I_s \text{ or } r_T = 0, \text{ any } I \\ 0 & \text{if } r_T > 0,\ I > I_s, \end{cases} \tag{63}$$

where I_s corresponds to the inflection point of f given by

$$I_s = \frac{1}{r_T}\log\left(\frac{1}{\gamma}\right). \tag{64}$$

Theorem 3 (*JC for Strong Toxicity and Slow Seed Growth*). *Let r_T be sufficiently large and g_S sufficiently small. Then, there exists a heteroclinic orbit in (32) from z_1^* to z_0^* for which the N-profile has a unique maximum, and the S-, A- and I-profiles are strictly monotonic.*

Proof. For asymptotically large r_T, the establishment function $f(I)$ (6) is exponentially close to 0 for $I > I_s + I_1$ and exponentially close to 1 for $I < I_s - I_1$, with $I_1 = (r_T)^{\alpha-1}$, for any $0<\alpha<1$. Moreover, both I_s (64) and I_1 are asymptotically close to zero.

For $f(I) \equiv 0$, the hyperplane $\{N=0\}$ is invariant under the flow of (32). Moreover, for this choice of f, the nontrivial equilibrium z_1^* lies on $\{N=0\}$, and is given by $\left(\frac{1-k_A}{k_S}, 0, 0, 1-k_A, \frac{1-k_A}{k_I}\right)$ (8). By Lemma's 1 and 2, we see that S, I and A are strictly monotonically decreasing on the invariant hyperplane $\{N=0\}$. Since $\{N=0\}$ is normally hyperbolic and $f(I)$ is asymptotically small for all $I > I_s + I_1$, the half-hyperplane $P_0 := \{N=0,\ I > I_s + I_1\}$ perturbs to a locally invariant codimension-1 manifold P for the full system (32) [36]. The unstable manifold of z_1^* of the flow on P, that we denote by $\mathcal{W}_P^u(z_1^*)$, is 3-dimensional. Since P is normally repelling in the N-direction, we can conclude that in a neighbourhood of P, the 4-dimensional unstable manifold of z_1^* in the full system (32) is foliated as $\mathcal{W}^u(z_1^*) = \mathcal{W}^u\left(\mathcal{W}_P^u(z_1^*)\right)$.

The A-dynamics on P are to exponential order in $\frac{1}{r_T}$ given by $A' + \frac{1}{c}A\left(1-k_A-A\right)=0$, which yield $A(\xi) = A(0)(1-k_A)\left[A_0 + (1-k_A-A_0)\, e^{\frac{1-k_A}{c}\xi}\right]^{-1}$. From the (linear) S- and I-dynamics on P, which depend linearly on A, we see that if $I \to I_s + I_1 = \mathcal{O}\left((r_T)^{\alpha-1}\right)$, then both $S \to S_1 = \mathcal{O}\left((r_T)^{\alpha-1}\right)$ and $A \to A_1 = \mathcal{O}\left((r_T)^{\alpha-1}\right)$; the same holds for the derivatives u and v. Moreover, in a sufficiently small neighbourhood of P, the normal N-dynamics are to leading order linear, and $N(\xi) = N_1 e^{\frac{k_N+g_A}{c}\xi}$ for N_1 sufficiently small.

We investigate the intersection of $\mathcal{W}^u(z_1^*)$ and $\mathcal{W}^s(z_0^*)$ in a neighbourhood of P, and in a neighbourhood of $I = I_s$. Close to both P and I_s, the S-, u-, A-, I-, and v-components of orbits in $\mathcal{W}^u(z_1^*)$ are $\mathcal{O}\left((r_T)^{\alpha-1}\right)$, while N is sufficiently small by assumption. Hence, in order for $\mathcal{W}^s(z_0^*)$ to intersect $\mathcal{W}^u(z_1^*)$ in this neighbourhood, all components of $\mathcal{W}^s(z_0^*)$ must be close to zero. It follows that the if intersection of $\mathcal{W}^s(z_0^*)$ and $\mathcal{W}^u(z_1^*)$ lies close to P and I_s, it has to be close to the origin z_0^*. Close to the origin, the dynamics on $\mathcal{W}^s(z_0^*)$ are linear, and $\mathcal{W}^s(z_0^*)$ is close to $E^s(z_0^*)$. Hence, for r_T sufficiently large, transversal intersections of $E^s(z_0^*)$ and $\mathcal{W}^u(z_1^*)$ perturb regularly to transversal intersections of $\mathcal{W}^s(z_0^*)$ and $\mathcal{W}^u(z_1^*)$.

Now, let $g_S \ll 1$. For $g_S = 0$, the flow of (32) is equal to the flow of (32) under the assumption $f(I) \equiv 0$. Hence, the hyperplane $\{N=0\}$ is invariant when $g_S = 0$. Moreover, the trivial equilibrium z_0^* lies on $\{N=0\}$. Solving the equations for A, S and I on $\{N=0\}$ yields the following unique heteroclinic orbit from z_1^* to z_0^* on $\{N=0\}$:

$$A_h(\xi) = A(0)(1-k_A)\left[A_0 + (1-k_A-A_0)e^{\frac{1-k_A}{c}\xi}\right]^{-1},$$

$$S_h(\xi) = e^{\mu_1^-\xi}\int_{-\infty}^{\xi} A(\zeta)\,\frac{e^{-\mu_1^-\zeta}}{\mu_1^+-\mu_1^-}\,\mathrm{d}\zeta + e^{\mu_1^+\xi}\int_{\xi}^{+\infty} A(\zeta)\,\frac{e^{-\mu_1^+\zeta}}{\mu_1^+-\mu_1^-}\,\mathrm{d}\zeta,$$

$$I_h(\xi) = e^{\lambda_1^-\xi}\int_{-\infty}^{\xi} A(\zeta)\,\frac{e^{-\lambda_1^-\zeta}}{\lambda_1^+-\lambda_1^-}\,\mathrm{d}\zeta + e^{\lambda_1^+\xi}\int_{\xi}^{+\infty} A(\zeta)\,\frac{e^{-\lambda_1^+\zeta}}{\lambda_1^+-\lambda_1^-}\,\mathrm{d}\zeta,$$

cf. Lemma 1. Thus, for $g_S = 0$, $\mathcal{W}^s(z_0^*)$ and $\mathcal{W}^u(z_1^*)$ intersect transversally in the hyperplane $\{N=0\}$, and this intersection is one-dimensional.

We investigate how this intersection perturbs for $0 < g_S \ll 1$. As the term $g_S\, S\, f(I)$ is a regular perturbation of system (32), we know that both the hyperplane $\{N=0\}$ and the stable/unstable manifolds of the equilibria $z_{0,1}^*$ perturb regularly in g_S. To determine the N-profile, we consider the unstable eigenvalues λ_1^-, λ_2^- and $\tilde{\lambda}_2$ of z_0^* (cf. the proof of Theorem 1), which for $0 < g_s \ll 1$ can be determined explicitly: we find $\lambda_1^- = -\frac{1}{2d^2}\left(-c-\sqrt{c^2+4d^2k_I}\right)$ (38), $\lambda_2^- = \mu_1^- + \mathcal{O}(g_S)$ (61) and $\tilde{\lambda}_2 = \frac{1-kA}{c} + \mathcal{O}(g_S)$, cf. (37)–(39). The associated eigenvectors can be determined by an expansion in powers of g_S. To leading order, the N-component of the eigenvectors is zero, due to the fact that the intersection of $\mathcal{W}^s(z_0^*)$ and $\mathcal{W}^u(z_1^*)$ lies in the $\{N=0\}$ hyperplane for $g_S = 0$. The first order correction of the eigenvectors associated to λ_2^- and $\tilde{\lambda}_2$ yields a nonzero N-component, to wit $\frac{g_S}{1+\gamma}\frac{1}{g_A+k_N-c\mu_1^-}$ for the λ_2^--eigenvector and $\frac{g_S}{1+\gamma}\frac{1}{g_A+k_N+1-k_A}\frac{1-k_A+k_I-d^2\frac{(1-k_A)^2}{c^2}}{1-k_A+k_S-\frac{(1-k_A)^2}{c^2}}$ for the $\tilde{\lambda}_2$-eigenvector. Hence, to first order in g_S, the N-profile is exponentially decreasing as $\xi \to \infty$, along these eigenvectors.

Now, define ξ_* through $I_h(\xi_*) = I_s$ (64). Note that ξ_* is well-defined since I_h is strictly monotonically decreasing when I_h is sufficiently small (Lemma 1). I is to exponential accuracy in $\frac{1}{r_T}$ approximated by I_h on P, (at least) up to $I = I_s + I_1$. In addition, I is to leading order in g_S approximated by the linear dynamics on $E^s(z_0^*)$, (at least) up to

$I_s - I_1$. The change of I over the interval $(I_s - I_1, I_s + I_1)$ is small, and since system (32) is regularly perturbed for small g_S and large r_T, this implies that the change in all other components over the ξ-interval associated to the change from $I = I_s + I_1$ to $I = I_s - I_1$ is small as well. Hence, to leading order, we can match the linear dynamics on $E^s(z_0^*)$ to the dynamics of $\mathcal{W}^u\left(\mathcal{W}^u_P(z_1^*)\right)$ at $\xi = \xi_*$. The transversality of the intersection of $\mathcal{W}^s(z_0^*)$ and $\mathcal{W}^u(z_1^*)$ ensures that this matching procedure can be carried out for every component. The result for the N-profile is a single peak, to leading order in g_S up to $\xi = \xi_*$ determined by the exponential increase with rate $\frac{k_N + g_A}{c}$ along the unstable fibres of $\mathcal{W}^u\left(\mathcal{W}^u_P(z_1^*)\right)$, and from $\xi = \xi_*$ onwards determined by the exponential decrease along $E^s(z_0^*)$, with exponential rates given by the stable eigenvalues λ_2^- and $\tilde{\lambda}_2$. □

Remark 3. While the condition $r_T \gg 1$ in Theorem 3 is natural (sufficiently strong toxicity feedback induces a JC distribution), the second condition $g_S \ll 1$ seems less so. Indeed, the necessity for this condition is purely technical, as it allows us to obtain analytical expressions for the stable eigenvalues and eigenvectors of z_0^* (39). However, considering the feasible parameter ranges for g_S, and in particular for the product $g_A g_N g_S$, we infer from Table 2 that $g_A g_N g_S$ is small for a significant subset of parameter space — that is, for most values of g_A and g_N, the condition that g_S is sufficiently small is not restrictive.

5.5. Wave speed

The analysis of front propagation in excitable media has been a topic of interest for several decades. In his seminal review paper, Van Saarloos [35] used the characterisation *pulled front* for those travelling fronts whose speed is determined by the instability of the spatially homogeneous steady state that is being invaded.

In this section, we analytically determine this 'linear' speed a pulled front would have, by a linear analysis near $\mathcal{E}_0^*$. To determine whether the numerically observed fronts can indeed be classified as 'pulled', we then compare c_* with the wave speed computed numerically for the emerging travelling wave solutions.

Theorem 4. *The linear wave speed c_* of a pulled front solution to Eq. (3) is given by*

$$c_* = \frac{d\omega_3}{d\kappa}(\kappa_*) \tag{65}$$

where $\omega_3(\kappa) \in \mathbb{C}$ is a purely imaginary solution to

$$\frac{g_A\, g_N\, g_S}{1+\gamma} + (1 - k_A + i\,\omega)(i\,\omega - g_A - k_N)(i\,\omega - k_S - \kappa^2) = 0 \tag{66}$$

and $\kappa_* = i\,\beta_*^+$ with $\beta_*^+ > 0$ solution to

$$\frac{d\omega_3}{d\kappa}(i\,\beta_*) = \frac{\mathrm{Im}(\omega_3(i\,\beta_*))}{\beta_*}. \tag{67}$$

Proof. In order to compute the linear wave speed, we analyse the dispersion relation of Fourier modes of the linearisation of Eq. (3) at $\mathcal{E}_0^*$. Introducing the diffusion matrix

$$\mathcal{D} := \begin{pmatrix} 1 & 0 & 0 & 0 \\ 0 & 0 & 0 & 0 \\ 0 & 0 & 0 & 0 \\ 0 & 0 & 0 & d^2 \end{pmatrix}, \tag{68}$$

the dispersion relation $\omega = \omega(\kappa)$ is given by the solution to

$$\det\left(i\,\omega - \kappa^2 \mathcal{D} + J|_{\mathcal{E}_0^*}\right) = 0, \tag{69}$$

where $\omega \in \mathbb{C}$ represents the (generalised) frequency, $\kappa \in \mathbb{C}$ the (generalised) wave number, and $J|_{\mathcal{E}_0^*}$ is the Jacobian (21) evaluated at $\mathcal{E}_0^*$. In our case, Eq. (69) takes the form of the fourth order polynomial in ω

$$\left(i\,\omega - d^2\,\kappa^2 - k_I\right)\left(\frac{g_A\, g_N\, g_S}{1+\gamma} + (1 - k_A + i\,\omega)(i\,\omega - g_A - k_N) \times (i\,\omega - k_S - \kappa^2)\right) = 0. \tag{70}$$

For sake of simplicity, Eq. (70) can be equivalently expressed as $\varphi(\omega,\kappa)\cdot\psi(\omega,\kappa) = 0$, where

$$\varphi(\omega,\kappa) := \left(i\,\omega - d^2\,\kappa^2 - k_I\right),$$
$$\psi(\omega,\kappa) := \left(\frac{g_A\, g_N\, g_S}{1+\gamma} + (1 - k_A + i\,\omega)(i\,\omega - g_A - k_N)(i\,\omega - k_S - \kappa^2)\right). \tag{71}$$

Given a solution $\omega(\kappa)$ to Eq. (70), the linear wave speed $c_* \in \mathbb{R}$ and the linear spreading point κ_* associated to $\omega(\kappa)$ are given by the solutions to the equations

$$c_* = \frac{d\omega}{d\kappa}(\kappa_*) = \frac{\mathrm{Im}(\omega(\kappa_*))}{\mathrm{Im}(\kappa_*)}, \tag{72}$$

see [35,37].

Among the four roots $\omega_i(\kappa)$, $i = 1,\dots,4$ satisfying Eq. (70) we define $\omega_1(\kappa)$ as the unique root of $\varphi(\omega,\kappa)$ and $\omega_i(\kappa)$, $i = 2,3,4$ as the three roots of the cubic polynomial $\psi(\omega,\kappa)$. Since we have that $\omega_1 = -i\,(d^2\,\kappa^2 + k_I)$, we exclude this root from further analysis as ω_1 does not admit solutions to (72).

In our analysis of the other three roots $\omega_i(\kappa)$, $i = 2,3,4$ we introduce the additional assumption (based on our numerical findings, see below) that both ω and κ are purely imaginary, as the fronts we observe are monotonic, i.e. non-oscillatory, both in space and time, near the trivial steady state $\mathcal{E}_0^*$. In particular, spatial oscillations around $\mathcal{E}_0^*$ would violate the fundamental model assumption that all model components are non-negative. Hence, we write $\kappa = i\,\beta$ with $\beta \in \mathbb{R}$. We note that in this case Eq. (70) is explicitly solvable, however the analytical expression for c_* (function of $g_A\, g_N\, g_S$, $g_A + k_N$, and k_S) is a root of a fifth order polynomial, making it hardly accessible (and hence is not provided here). As observed numerically, two out of three roots $\omega_2(\kappa)$ and $\omega_4(\kappa)$ are not purely imaginary for every value of β, and are therefore further discarded from our investigation. The unique root $\omega_3(\kappa)$ is finally used to derive the value of $\kappa_* = i\,\beta_*$ such that Eq. (67) holds, i.e.

$$\frac{d\omega_3}{d\kappa}(i\,\beta_*) = \frac{\mathrm{Im}(\omega_3(i\,\beta_*))}{\beta_*}.$$

This equation admits two solutions $\beta_*^{\pm}$ with opposite signs; however, as we are interested in right-moving fronts, we only retain the positive solution $\beta_*^+ > 0$. We thus finally obtain the linear wave speed as

$$c_* = \frac{d\omega_3}{d\kappa}(i\,\beta_*^+) = \frac{\mathrm{Im}(\omega_3(i\,\beta_*^+))}{\beta_*^+}. \quad \square$$

As we do not provide an explicit analytical expression for $\omega_3(\kappa)$, in Fig. 6 we illustrate a typical plot of the functions $\frac{d\omega_3}{d\kappa}(i\,\beta)$ and $\frac{\mathrm{Im}(\omega_3(i\,\beta))}{\beta}$ with respect to β for the following fixed parameter values (within the ranges reported in Table 2):

$$g_A = 0.8, \quad g_N = 20, \quad \gamma = 10^{-5}, \quad k_A = 0.04, \quad k_N = 2, \quad k_S = 1.32. \tag{73}$$

5.5.1. Numerical investigation

In order to further validate the existence of pulled front solutions travelling with speed c_* as described in Theorem 4, we perform numerical simulations of System (1) on a one-dimensional domain of size $\hat{L} = 350$ m discretised with a spatial grid of $\hat{\delta x} = 0.1$ m and $m = 3500$ grid cells including Neumann boundary conditions and the following initial conditions

$$\hat{S}(x,0) = \hat{S}_0(x) = e^{-\frac{5(\hat{L}-2x)^2}{2\hat{L}}}, \quad \hat{N}(x,0) = \hat{A}(x,0) = \hat{I}(x,0) = 0, \tag{74}$$

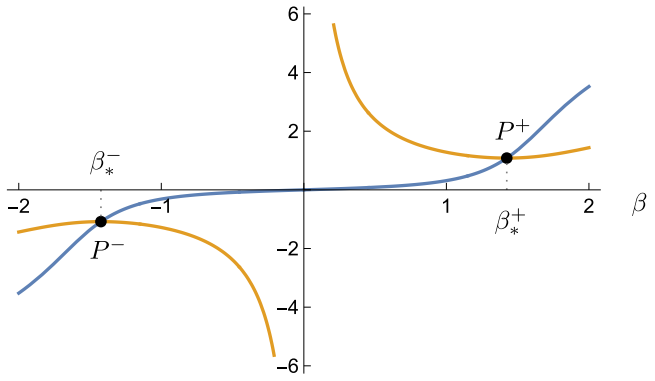

Fig. 6. Plot of the functions $\frac{d\omega_3}{dk}(i\beta)$ (blue curve) and $\frac{\mathrm{Im}(\omega_3(i\beta))}{\beta}$ (yellow curve) for parameter values as in Eq. (73) and $g_S = 0.132$. The intersection points between these two curves occurring at $\beta = \beta_*^{\pm}$ are indicated by the two black points $P^{\pm}$. For these parameter values we observe that $\beta_*^{\pm} \approx \pm 1.42$ and therefore $P^{\pm} = (\pm 1.42, \pm 1.08)$.

where the dimensional parameters correspond to the ones described in Table 1 The total simulation time is $\hat{\mathcal{T}} = 500$ years with timesteps of $\hat{\delta t} = 0.001$ years. Following [38], the numerical scheme used in our simulations is based on a forward Euler integration of the finite-difference equations obtained by discretising the diffusion operator with no-flux (i.e. Neumann) boundary conditions.

The dimensional parameter values fixed in this simulation (other than the ones already fixed in Table 1) are (for unit measures we refer to Table 1)

$$\hat{k}_S = 0.33, \quad \hat{g}_N = 5, \quad \hat{r}_T = 34, \quad \hat{k}_N = 0.5, \quad \hat{r}_P = 1, \quad \hat{g}_A = 0.2, \quad \hat{d}_I = 0.5. \tag{75}$$

We then investigate two aspects, namely the dependency of the wave speed on the parameter $\hat{g}_S$ (fixing $\hat{d}_S = 0.6$) and the dependency of the wave speed on $\hat{d}_S$ (fixing $\hat{g}_S = 0.033$).

A comparison between the values of the linear wave speed obtained from the analytical investigation described in Theorem 4 and the numerical speed computed by means of simulations w.r.t. g_S and d is given in Fig. 7. To obtain it, we first calculate the dimensional wave speed $\hat{c}_*$ as follows, and then derive the nondimensional wave speed as $c_* = \sqrt{\frac{\hat{c}_A}{\hat{d}_S}}\,\hat{c}_*$. The dimensional numerical wave speed $\hat{c}_*$ in both scenarios described above – identified by $\hat{c}_*^{\hat{g}_S}$ and $\hat{c}_*^{\hat{d}_S}$, respectively – is obtained by tracking at each time $\hat{t}_j = j \cdot \hat{\delta t}$ the location of the inflection point in the $\hat{A}$ profile – defined as $\hat{x}_j$ – and subsequently calculating the mean of the difference quotient over a specific range of iterations, namely

$$\begin{aligned} \hat{c}_*^{\hat{g}_S} &:= \frac{1}{479} \sum_{j=20}^{498} \frac{\hat{x}_{j+1} - \hat{x}_j}{\hat{t}_{j+1} - \hat{t}_j}, \\ \hat{c}_*^{\hat{d}_S} &:= \frac{1}{n(\hat{d}_S)} \sum_{j=50}^{\theta(\hat{d}_S)} \frac{\hat{x}_{j+1} - \hat{x}_j}{\hat{t}_{j+1} - \hat{t}_j}, \end{aligned} \tag{76}$$

where

$$\theta(\hat{d}_S) := -38.76\, \hat{d}_S^3 + 266.946\, \hat{d}_S^2 - 619.173\, \hat{d}_S + 662.244. \tag{77}$$

The function $\theta(\hat{d}_S)$ has been derived by interpolating end times in the simulations such that a wave travels with constant shape for $j = 50, \ldots, \theta(\hat{d}_S)$. This is due to the fact that the range of $\hat{d}_S$ over which the simulation runs has a strong impact on the speed of the travelling wave, which reaches the boundary of the spatial domain sooner for higher values of $\hat{d}_S$. The number of iterations $n(\hat{d}_S)$ over which the speed $\hat{c}_*^{\hat{d}_S}$ is calculated hence varies with $\hat{d}_S$. Since, on the other hand, variations of $\hat{g}_S$ do not exhibit the same properties, the interval over which the numerical wave speed is calculated is here considered as constant.

By converting the numerical wave speed in Eq. (76) in its nondimensional form $c_*^{g_S}$ and c_*^{d}, we finally compare it with the analytical values obtained in Theorem 4 (see Fig. 7). We note that the strong dependency of the dimensional wave speed $\hat{c}_*^{\hat{d}_S}$ on $\hat{d}_S$ does not imply that the same effect should be valid for the nondimensional speed, which in fact remains approximately constant as d varies as shown in Fig. 7(b).

We finally observe that the numerical results confirm (up to $\mathcal{O}(10^{-2})$ due to numerical precision) the analytical predictions; such accuracy increases by increasing the size of the domain (by considering larger values of m) and thus increasing simulation times as well (see Fig. 8). In order to achieve even higher accuracy, the size of the domain should increase with $\hat{d}_S$ since (as discussed above) for higher values of the seed dispersal coefficient the boundary of the spatial domain is reached sooner by the travelling wave (we note that larger values of $\hat{d}_S$ correspond to lower values of its nondimensional counterpart d).

6. Conclusion

In this work, we have introduced a novel reaction–diffusion-ODE model for (ecologically relevant) transient patterns observed in nature, known as Janzen–Connell distributions. The functional responses adopted in the model, as well as the parameter ranges chosen for the analysis, are based on theoretical assumptions supported by experimental findings [14,39–41]. We have included two prominent mechanisms in negative plant–soil feedback, namely growth inhibition and increased mortality, in order to show their key role in the emergence of such transient patterns.

The analytical challenges provided by the complex structure of some functional responses, in particular the germination function, were here overcome by exploiting the small scale of certain parameters in the system. This feature has also played a key role in our thorough investigation of travelling wave solutions, i.e. the theoretical representation of the JC distributions we aimed to describe. Our linear stability analysis allowed us to rule out the existence of Turing bifurcations and infer the existence of travelling wave solutions for parameter values spanning within ranges of ecological feasibility exhibiting the typical features of JC distributions. Moreover, numerical simulations suggested that the travelling wave solutions admitted by our model in a large area of parameter space correspond to pulled fronts, "pulled" by the linear spreading of small perturbations into the linearly unstable bare soil steady state. The analytical expression for the linear spreading speed was then compared with the numerical speed of one-dimensional waves travelling on a sufficiently large spatial domain, mimicking the unbounded domain of the analytical investigation; the high accuracy revealed by this comparison strongly supports our hypothesis on the pulled nature of the constructed fronts.

Previous ecological studies have highlighted the possibility of negative plant–soil feedback driving spatially regular pattern formation, associated with Turing instabilities of mean field states [42,43]. These previous studies, however, did not consider tree life-stage structure, despite its importance for the mechanisms at play [1,2]. Interestingly, we found that in our stage-structured model, there was no possibility of a Turing bifurcation providing the onset of spatially regular pattern formation. Our results highlight that future ecological studies may need to consider the effect of plant–soil feedbacks in different tree life stages explicitly, in order to infer their consequences for emergent spatio-temporal dynamics. Furthermore, our results are in line with previous ecological model studies showing that a plant invasion travelling wave only constitutes a 'pushed' front under strong positive plant–soil feedback [44]. In the cases of negative plant–soil feedback considered in this study, only 'pulled' fronts emerge. Whether this strong link between Janzen–Connell distributions and 'pulled' invasion fronts is

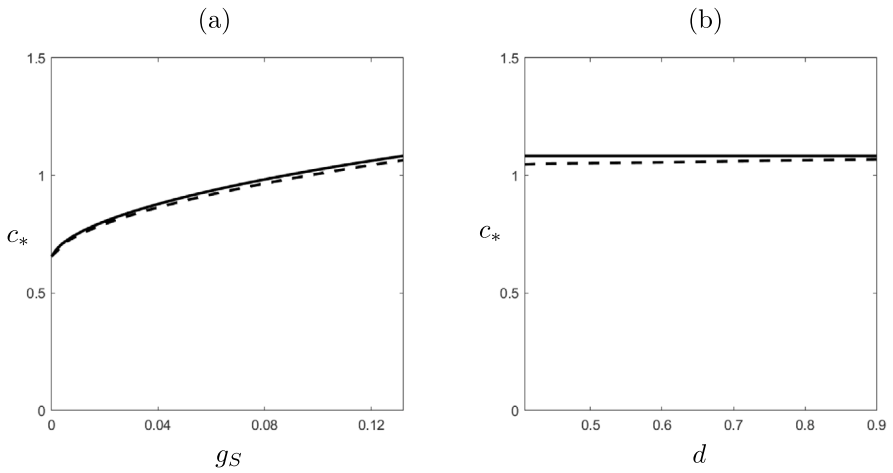

Fig. 7. Comparison between the nondimensional wave speed obtained analytically (solid line) and from numerical simulations (dashed line) as a function of (a) g_S with $d = 0.913$ and (b) d with $g_S = 0.132$. The other parameter values are set as in Eq. (73) together with $r_T = 4080$, $r_P = 480$. We note that these values are obtained by plugging the dimensional values in Eq. (75) into Eq. (4). The range of g_S (a) and d (b) correspond with the ranges of these parameters given in Table 2.

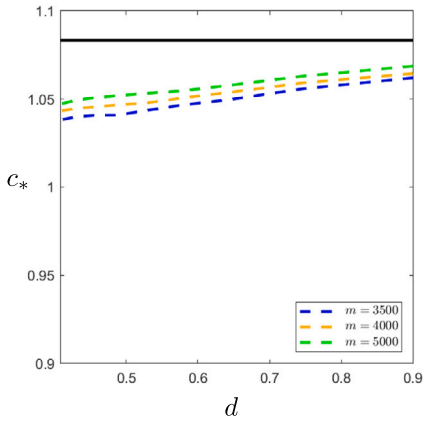

Fig. 8. Comparison between the wave speed obtained analytically (solid black line) and from numerical simulations (dashed lined) with the same parameter values as in Fig. 7 for different domain sizes $\hat{L} = m \cdot \hat{\delta x}$ with $m = 3500$ (blue), $m = 4000$ (orange), and $m = 5000$ (green). We note that the accuracy of the numerical wave speed increases with m.

robust to variations in model framework is an interesting avenue for further ecological studies.

As the presented model exhibits a rich and complex structure, several interesting research directions can be further considered. Few examples which we plan to undertake in the future include a deeper investigation of different scenarios corresponding to different combinations of growth inhibition/increased mortality intensity (represented by high/low values of r_T and r_P, respectively). Moreover, in order to increase the impact of our model beyond the theoretical sphere, we aim to focus on more realistic ecological scenarios where different trees interact in a limited space (i.e. a bounded domain) and, as a further step, extend our model to a multi-species framework.

Declaration of competing interest

The authors declare no competing interest.

Data availability

No data was used for the research described in the article.

Acknowledgements

AI is member of Gruppo Nazionale per la Fisica Matematica (GNFM), Istituto Nazionale di Alta Matematica (INdAM). AI acknowledges support from an FWF Hertha Firnberg Research Fellowship (10.55776/T1199). MB acknowledges the Italian National Biodiversity Future Center (NBFC): National Recovery and Resilience Plan (NRRP), Mission 4 Component 2 Investment 1.4 of the Italian Ministry of University and Research; funded by the European Union - NextGenerationEU (Project code $CN_0$0000033).

Appendix. Linear stability of $\mathcal{E}_1^*$ with respect to spatially homogeneous perturbations for $\eta, \zeta \neq \mathcal{O}(1)$

Based on the values reported in Table 2, and observing that the maximum of $\left|f'\left(\frac{1}{k_I}\right)\right|$ is realised at $I = I_s$ and $\left|f'\left(\frac{1}{k_I}\right)\right|_{\max} = \frac{k_I}{4}\log\left(\frac{1}{\gamma}\right)$, we have that the parameters η and ζ in (25) can vary within the following ranges:

$$\eta \in \left(0,\, 3.6 \cdot 10^2\right), \qquad \zeta \in \left(0,\, 3.2 \cdot 10^2\right).$$

The linear stability of the steady state $\mathcal{E}_1^*$ w.r.t. homogeneous perturbations in the case of $\eta, \zeta \in \mathcal{O}(1)$ has been discussed in the proof of Proposition 2. Here, we look at the other possible regimes, i.e.

I. $\eta \gg 1$, $\zeta \in \mathcal{O}(1)$,
II. $\eta \in \mathcal{O}(1)$, $\zeta \gg 1$,
III. $\eta, \zeta \gg 1$.

A.1. Regime I: $\eta \gg 1$, $\zeta \in \mathcal{O}(1)$

In this case, the dominant term in the characteristic polynomial (26) becomes

$$p_1(\lambda) = \eta\, \left(k_S + \lambda\right)\left(k_I + \lambda\right)\left(\frac{1}{\delta} + \lambda\right) + \mathcal{O}(1) + \mathcal{O}(\eta\, k_A)$$

when $\lambda \in \mathcal{O}(1)$, which implies that the eigenvalues $-k_s$, $-k_I$, and $-\frac{1}{\delta}$ perturb regularly. On the other hand, when $|\lambda| \gg 1$ dominant balance gives

$$\eta\, \lambda^3 + \lambda^4 + \mathcal{O}(\eta\, k_A\, \lambda^3) = 0$$

i.e. $\lambda = -\eta$ at leading order. In conclusion, all eigenvalues perturb regularly and remain negative.

A.2. Regime II: $\eta \in \mathcal{O}(1)$, $\zeta \gg 1$

Here, the characteristic polynomial is linear in ζ and is given by

$$p_1(\lambda) = q(\lambda) + \left(k_S + \lambda\right)\left(\delta\, k_A - \delta^2 k_A^2\right)\,\zeta, \tag{A.1}$$

where $q(\lambda)$ is a polynomial of degree four in λ. By writing $\zeta = \zeta_0\, k_A^{-y}$, we have that:

- if $0 \le y < 1$, the eigenvalues $-k_s$, $-k_I$, $-\frac{1}{\delta}$, and $-\left(k_N + \eta\right)$ perturb regularly;
- if $y = 1$, a regular expansion in k_A leads at leading order to the equation

$$\left(k_S + \lambda\right)\left(\delta\,\zeta_0 + \left(k_I + \lambda\right)\left(k_N + \eta + \lambda\right)\left(\frac{1}{\delta} + \lambda\right)\right) = 0, \tag{A.2}$$

  which implies that the eigenvalue $-k_S$ perturbs regularly, while the others shift above by $\mathcal{O}(1)$. These three eigenvalues are negative as long as ζ_0 remains below the Hopf bifurcation value ζ_0^H, which is found by imposing that the third order polynomial in Eq. (A.2) admits a purely imaginary root:

$$\zeta_0^H := \frac{1}{\delta^3}\left(k_N + k_I + \eta\right)\left(1 + \delta k_I\right)\left(1 + \delta\left(k_N + \eta\right)\right). \tag{A.3}$$

  This implies that, for any $\zeta = \frac{\zeta_0}{k_A} < \frac{\zeta_0^H}{k_A}$, we have three negative eigenvalues.
- if $y > 1$, we have that $-k_S$ is the only eigenvalue which perturbs regularly (i.e. $\lambda \in \mathcal{O}(1)$). On the other hand, dominant balance for $|\lambda| \gg 1$ leads to $\lambda^3 = -\delta\,\zeta\, k_A \gg 1$, which implies that here we have one real, negative eigenvalue and two complex conjugates eigenvalues with positive real part for any $\zeta \gg 1$.

In conclusion, in this case we have that all four roots of the polynomial in Eq. (A.1) are negative as long as $\zeta < \frac{1}{k_A}\,\zeta_0^H$.

A.3. Regime III: η, $\zeta \gg 1$

The characteristic polynomial in this last regime is given by

$$\begin{aligned} p_1(\lambda) = {} & \left(k_S + \lambda\right)\left(k_I + \lambda\right)\left(\frac{1}{\delta} + \lambda\right)\left(k_N + \eta + \lambda\right) \\ & + k_A\,\left(\delta\,\zeta\,\left(k_S + \lambda\right) + \mathcal{O}(\eta^0)\right. \\ & + \eta\left(k_I\,(1-\delta)\left(k_S + \lambda\right) - \left(k_I + \lambda\right)\left(k_S\,(2 + \delta\,\lambda)\right.\right. \\ & \left.\left. + \;\lambda\,(1 + \delta + \delta\,\lambda)\right)\right) + \mathcal{O}(\eta^0)\Big). \end{aligned} \tag{A.4}$$

As before, the eigenvalues $\lambda = -k_S < 0$ perturbs regularly, providing one stable, $\mathcal{O}(1)$ eigenvalue. In order to establish the nature of the other three eigenvalues we need to consider the following scenarios:

1. If $\eta \gg \zeta\, k_A$, the eigenvalues $\lambda = -k_I$ $\lambda = -\frac{1}{\delta}$ also perturb regularly, providing two negative $\mathcal{O}(1)$ eigenvalues; an additional negative $\mathcal{O}(\eta)$ eigenvalue is given by $\lambda = -\left(k_N + \eta\right)$, so in total we have here three stable eigenvalues.
2. If $\eta \sim \zeta\, k_A$, we can write $\zeta\, k_A = \zeta_0\,\eta$. Replacing this expression in Eq. (A.4) leads to two $\mathcal{O}(1)$ eigenvalues with negative real part obtained by solving $\delta\,\lambda^2 + \left(1 + \delta\, k_I\right)\lambda + \left(k_i + \delta^2\zeta_0\right) = 0$ (since $\left(1 + \delta\, k_I\right) > 0$) and one $\mathcal{O}(\eta)$ eigenvalue $\lambda = -\eta < 0$. Therefore, in this case we also have three stable eigenvalues.
3. If $\eta \ll \zeta\, k_A$, we have that $\delta\,\zeta\, k_A\left(1 - \delta\, k_A\right)\left(k_S + \lambda\right)$ balances $\lambda^4 + \lambda^3\left(\left(1 - \delta\, k_A\right)\eta + \mathcal{O}(\eta^0)\right) + \mathcal{O}(\lambda^0)$ in Eq. (A.4). This leads to further possible scenarios:

   (a) If $\lambda^4 \gg \lambda^3\eta$, the characteristic polynomial at leading order becomes $\lambda^4 + \delta\,\zeta\, k_A\,\lambda = 0$, whose nontrivial solutions consist in two complex roots with positive real part and one negative real root. This implies $\lambda^3 \sim \zeta\, k_A$. At the same time, in this case we have $\lambda \gg \eta$; these two considerations lead to $\zeta\, k_A \gg \eta^3$.

   (b) If $\lambda^4 \sim \lambda^3\eta$, we can write $\lambda = \lambda_0\,\eta$; plugging this into the dominant terms of the characteristic polynomial leads to $\zeta\, k_A \sim \eta^3$, hence we can write $\zeta\, k_A = \zeta_0\,\eta^3$. Including this further assumption, the roots of the characteristic polynomial are given by the solutions to $\lambda_0^3 + \lambda_0^2 + \delta\,\zeta_0 + \mathcal{O}(k_A) = 0$. In the case $\delta\,\zeta_0 = 0$, this polynomial admits the negative root $\lambda = -1$ and a double zero solution. Including the positive term $\delta\,\zeta_0$ hence implies that the negative root perturbs to a root which remains real and negative, whereas the double zero perturbs to a pair of complex conjugate roots with positive real part given by $\frac{\delta\,\zeta_0}{2}$ at leading order. In this case no Hopf bifurcation occurs, since the polynomial does not admit purely imaginary roots for any value of $\delta\,\zeta_0$. Therefore, here we have two stable and one unstable eigenvalues.

   (c) If $\lambda^4 \ll \lambda^3\eta$, the characteristic polynomial up to its dominant terms reduces to $\lambda^3\,\eta + \delta\,\zeta\, k_A\,\lambda = 0$ and is solved by $\lambda = \pm i\left(\frac{\delta\,\zeta\, k_A}{\eta}\right)^{1/2}$, hence requires further unfolding. First, however, we observe that here $\lambda^2 \sim \frac{\zeta\, k_A}{\eta}$, which implies $\zeta\, k_A \gg \left(\frac{\zeta\, k_A}{\eta}\right)^{3/2}$ and, in turn, that this scenario corresponds to $\zeta\, k_A \ll \eta^3$. Considering higher order terms leads to the following subcases:

      i If $\eta \ll \zeta\, k_A \ll \eta^2$, the characteristic polynomial admits two roots with negative real part given by

$$\lambda = \pm i\left(\frac{\delta\,\zeta\, k_A}{\eta}\right)^{1/2} - \frac{\sqrt{\delta}}{2}\,\frac{\zeta\, k_A}{1 - \delta\, k_A}\,\frac{1}{\eta^{9/2}}.$$

      ii If $\eta^2 \ll \zeta\, k_A \ll \eta^3$, the characteristic polynomial admits two roots with positive real part given by

$$\lambda = \pm i\left(\frac{\delta\,\zeta\, k_A}{\eta}\right)^{1/2} + \frac{1}{2\,\delta^{3/2}}\left(1 + \delta\, k_I - \delta^2 k_A\right)\,\frac{1}{\eta^{5/2}}.$$

      iii If $\eta^2 \sim \zeta\, k_A$, writing $\zeta\, k_A = \zeta_0\,\eta^2$ leads to the following two roots of the characteristic polynomial with positive real part, given by

$$\lambda = \pm i\left(\delta\,\eta\,\zeta_0\right)^{1/2} + \frac{\left(1 - \delta\, k_A\right)\left(1 - \delta\, k_I + \delta^2 k_A\right) + \delta^2\zeta_0}{2\,\delta^{3/2}\,\eta^{5/2}\left(1 - \delta\, k_A\right)}.$$

      A Hopf bifurcation occurs at

$$\hat{\zeta}_0^H = \frac{1 + \delta\, k_I}{\delta^2} + \mathcal{O}(k_A).$$

To summarise, in this case we have that the four eigenvalues of the characteristic polynomial are negative – i.e. $\mathcal{E}_1^*$ is stable to homogeneous perturbations – as long as $\zeta < \frac{\eta^2}{k_A}\,\hat{\zeta}_0^H + \mathcal{O}(1)$. We observe that this value corresponds to the leading order term of $\frac{1}{k_A}\,\zeta_0^H$ for large η, i.e. regime II converges to regime III as $\eta \to \infty$ as expected.

References

[1] J.H. Connell, On the role of natural enemies in preventing competitive exclusion in some marine animals and in rain forest trees, Dyn. Popul. 298 (312) (1971).

[2] D.H. Janzen, Herbivores and the number of tree species in tropical forests, Amer. Nat. 104 (940) (1970) 501–528, http://dx.doi.org/10.1086/282687.

[3] R. Macarthur, R. Levins, The limiting similarity, convergence, and divergence of coexisting species, Amer. Nat. 101 (921) (1967) 377–385, http://dx.doi.org/10.1086/282505.

[4] R.M. May, Qualitative stability in model ecosystems, Ecology 54 (3) (1973) 638–641, http://dx.doi.org/10.2307/1935352.

[5] J.D. Bever, S.A. Mangan, H.M. Alexander, Maintenance of plant species diversity by pathogens, Annu. Rev. Ecol. Evol. Syst. 46 (2015) 305–325.

[6] T. Levi, M. Barfield, S. Barrantes, C. Sullivan, R.D. Holt, J. Terborgh, Tropical forests can maintain hyperdiversity because of enemies, Proc. Natl. Acad. Sci. 116 (2) (2018) 581–586, http://dx.doi.org/10.1073/pnas.1813211116.

[7] A. Packer, K. Clay, Soil pathogens and spatial patterns of seedling mortality in a temperate tree, Nature 404 (6775) (2000) 278–281.

[8] S.A. Mangan, S.A. Schnitzer, E.A. Herre, K.M.L. Mack, M.C. Valencia, E.I. Sanchez, J.D. Bever, Negative plant–soil feedback predicts tree-species relative abundance in a tropical forest, Nature 466 (7307) (2010) 752–755.

[9] L. Mari, R. Casagrandi, M. Gatto, T. Avgar, R. Nathan, Movement strategies of seed predators as determinants of plant recruitment patterns, Amer. Nat. 172 (5) (2008) 694–711, http://dx.doi.org/10.1086/591687.

[10] L. Mari, M. Gatto, R. Casagrandi, Central-place seed foraging and vegetation patterns, Theor. Popul. Biol. 76 (4) (2009) 229–240, http://dx.doi.org/10.1016/j.tpb.2009.08.001.

[11] R. Nathan, R. Casagrandi, A simple mechanistic model of seed dispersal, predation and plant establishment: Janzen-Connell and beyond, J. Ecol. 92 (5) (2004) 733–746.

[12] S. Thompson, P. Alvarez-Loayza, J. Terborgh, G. Katul, The effects of plant pathogens on tree recruitment in the Western Amazon under a projected future climate: a dynamical systems analysis, J. Ecol. 98 (6) (2010) 1434–1446, http://dx.doi.org/10.1111/j.1365-2745.2010.01726.x.

[13] G. Bonanomi, M. Zotti, M. Idbella, P. Termolino, V. De Micco, S. Mazzoleni, Field evidence for litter and self-DNA inhibitory effects on Alnus glutinosa roots, New Phytol. 236 (2) (2022) 399–412, http://dx.doi.org/10.1111/nph.18391.

[14] S. Mazzoleni, G. Bonanomi, G. Incerti, M.L. Chiusano, V. Lanzotti, et al., Inhibitory and toxic effects of extracellular self-DNA in litter: a mechanism for negative plant-soil feedbacks? New Phytol. 205 (3) (2014) 1195–1210, http://dx.doi.org/10.1111/nph.13121.

[15] G. Bonanomi, F. Giannino, S. Mazzoleni, Negative plant-soil feedback and species coexistence, Oikos 111 (2) (2005) 311–321, http://dx.doi.org/10.1111/j.0030-1299.2005.13975.x.

[16] S. Mazzoleni, G. Bonanomi, F. Giannino, G. Incerti, S.C. Dekker, M. Rietkerk, Modelling the effects of litter decomposition on tree diversity patterns, Ecol. Model. 221 (23) (2010) 2784–2792, http://dx.doi.org/10.1016/j.ecolmodel.2010.08.007.

[17] S. Mazzoleni, G. Bonanomi, F. Giannino, M. Rietkerk, S. Dekker, F. Zucconi, Is plant biodiversity driven by decomposition processes? An emerging new theory on plant diversity, Community Ecol. 8 (1) (2007) 103–109, http://dx.doi.org/10.1556/comec.8.2007.1.12.

[18] G. Bonanomi, G. Incerti, A. Stinca, F. Cartenì, F. Giannino, S. Mazzoleni, Ring formation in clonal plants, Community Ecol. 15 (1) (2014) 77–86, http://dx.doi.org/10.1556/comec.15.2014.1.8.

[19] F. Cartenì, A. Marasco, G. Bonanomi, S. Mazzoleni, M. Rietkerk, F. Giannino, Negative plant soil feedback explaining ring formation in clonal plants, J. Theoret. Biol. 313 (2012) 153–161, http://dx.doi.org/10.1016/j.jtbi.2012.08.008.

[20] N. Karst, D. Dralle, S. Thompson, Spiral and rotor patterns produced by fairy ring fungi, in: Jordi Garcia-Ojalvo (Ed.), PLoS One 11 (3) (2016) e0149254, http://dx.doi.org/10.1371/journal.pone.0149254.

[21] N. Salvatori, M. Moreno, M. Zotti, A. Iuorio, F. Cartenì, G. Bonanomi, S. Mazzoleni, F. Giannino, Process based modelling of plants-fungus interactions explains fairy ring types and dynamics, SSRN Electron. J. (2022) http://dx.doi.org/10.2139/ssrn.4137982.

[22] A. Marasco, F. Giannino, A. Iuorio, Modelling competitive interactions and plant–soil feedback in vegetation dynamics, Ric. Mat. 69 (2) (2020) 553–577, http://dx.doi.org/10.1007/s11587-020-00497-6.

[23] A. Marasco, A. Iuorio, F. Cartenì, G. Bonanomi, D.M. Tartakovsky, S. Mazzoleni, F. Giannino, Vegetation pattern formation due to interactions between water availability and toxicity in plant–soil feedback, Bull. Math. Biol. 76 (11) (2014) 2866–2883, http://dx.doi.org/10.1007/s11538-014-0036-6.

[24] S. Härting, A. Marciniak-Czochra, I. Takagi, Stable patterns with jump discontinuity in systems with Turing instability and hysteresis, Discrete Contin. Dyn. Syst. 37 (2) (2016) 757–800.

[25] A. Iuorio, F. Veerman, The influence of autotoxicity on the dynamics of vegetation spots, Physica D 427 (2021) 133015.

[26] A. Köthe, A. Marciniak-Czochra, I. Takagi, Hysteresis-driven pattern formation in reaction-diffusion-ODE systems, Discrete Contin. Dyn. Syst. 40 (6) (2020) 3595–3627.

[27] A. Marciniak-Czochra, G. Karch, K. Suzuki, Instability of Turing patterns in reaction-diffusion-ODE systems, J. Math. Biol. 74 (2017) 583–618.

[28] F. Veerman, M. Mercker, A. Marciniak-Czochra, Beyond Turing: far-from-equilibrium patterns and mechano-chemical feedback, Phil. Trans. R. Soc. A 379 (2213) (2021) 20200278.

[29] S. Brown, J. Dockery, M. Pernarowski, Traveling wave solutions of a reaction diffusion model for competing pioneer and climax species, Math. Biosci. 194 (1) (2005) 21–36.

[30] P. Gerlee, S. Nelander, Travelling wave analysis of a mathematical model of glioblastoma growth, Math. Biosci. 276 (2016) 75–81.

[31] K. Harley, P. van Heijster, R. Marangell, G.J. Pettet, M. Wechselberger, Numerical computation of an Evans function for travelling waves, Math. Biosci. 266 (2015) 36–51.

[32] C.E. Vincenot, F. Cartenì, G. Bonanomi, S. Mazzoleni, F. Giannino, Plant-soil negative feedback explains vegetation dynamics and patterns at multiple scales, Oikos 126 (9) (2017) 1319–1328, http://dx.doi.org/10.1111/oik.04149.

[33] A. Iuorio, M.B. Eppinga, M. Baudena, F. Veerman, M. Rietkerk, F. Giannino, Modelling how negative plant-soil feedbacks across life stages affect the spatial patterning of trees, Nature Scientific Reports 13 (2023) 19128, http://dx.doi.org/10.1038/s41598-023-44867-0.

[34] K.J. Feeley, S. Joseph Wright, M.N. Nur Supardi, A.R. Kassim, S.J. Davies, Decelerating growth in tropical forest trees, Ecol. Lett. 10 (6) (2007) 461–469.

[35] W. van Saarloos, Front propagation into unstable states, Phys. Rep. 386 (2–6) (2003) 29–222, http://dx.doi.org/10.1016/j.physrep.2003.08.001.

[36] C. Kuehn, General Fenichel Theory, in: Multiple Time Scale Dynamics, Springer, ISBN: 978-3-319-12316-5, 2015, pp. 19—51, http://dx.doi.org/10.1007/978-3-319-12316-5_2.

[37] C. Kuehn, PDE Dynamics: An Introduction, Vol. 23, SIAM, 2019.

[38] M. Rietkerk, M.C. Boerlijst, F. van Langevelde, R. HilleRisLambers, J. van de Koppel, L. Kumar, H.H.T. Prins, A.M. de Roos, Self-organization of vegetation in arid ecosystems, Amer. Nat. 160 (4) (2002) 524, http://dx.doi.org/10.2307/3079239.

[39] Liza S Comita, Helene C Muller-Landau, Salomón Aguilar, Stephen P Hubbell, Asymmetric density dependence shapes species abundances in a tropical tree community, Science 329 (5989) (2010) 330–332.

[40] S.A. Mangan, S.A. Schnitzer, E.A. Herre, K.M.L. Mack, M.C. Valencia, E.I. Sanchez, J.D. Bever, Negative plant–soil feedback predicts tree-species relative abundance in a tropical forest, Nature 466 (7307) (2010) 752–755, http://dx.doi.org/10.1038/nature09273.

[41] Joseph A LaManna, Scott A Mangan, Alfonso Alonso, Norman A Bourg, Warren Y Brockelman, Sarayudh Bunyavejchewin, Li-Wan Chang, Jyh-Min Chiang, George B Chuyong, Keith Clay, et al., Plant diversity increases with the strength of negative density dependence at the global scale, Science 356 (6345) (2017) 1389–1392.

[42] Inderjit, Ragan M. Callaway, Ehud Meron, Belowground feedbacks as drivers of spatial self-organization and community assembly, Phys. Life Rev. 38 (2021) 1–24, http://dx.doi.org/10.1016/j.plrev.2021.07.002.

[43] M.B. Eppinga, W.H. Van der Putten, J.D. Bever, Plant-soil feedback as a driver of spatial structure in ecosystems: A commentary on "Belowground feedbacks as drivers of spatial self-organization and community assembly" by Inderjit, agan M. Callaway and Ehud Meron, Phys. Life Rev. 40 (2022) 6–14.

[44] Jonathan M. Levine, Elizaveta Pachepsky, Bruce E. Kendall, Stephanie G. Yelenik, Janneke Hille Ris Lambers, Plant-soil feedbacks and invasive spread, Ecol. Lett. 9 (9) (2006) 1005–1014, http://dx.doi.org/10.1111/j.1461-0248.2006.00949.x.